Citation
Vo, N.H. and Pham, T.M. and Hao, H. and Bi, K. and Chen, W. 2022. A reinvestigation of the spring-mass model for metamaterial bandgap prediction. International Journal of Mechanical Sciences. 221: ARTN 107219. http://doi.org/10.1016/j.ijmecsci.2022.107219

A Reinvestigation of the Spring-Mass Model for Metamaterial Bandgap Prediction

Nhi H. Vo[1], Thong M. Pham[2], Hong Hao[3], Kaiming Bi[4], and Wensu Chen[5]

Center for Infrastructural Monitoring and Protection, School of Civil and Mechanical Engineering, Curtin University, Kent Street, Bentley, WA 6102, Australia

Abstract

Metaconcrete and meta-truss bar are a new type of material and structure with extraordinary characteristics that cannot be found in nature. Metamaterials/metastructures possess the ability to manipulate wave propagation in certain frequency ranges, termed as bandgaps. Application of metamaterials/metastructures for structural protection is different from the traditional strategies which resist the external loads by using their strength or energy absorption through plastic deformation, metamaterials and/or metastructures stop incident stress waves from propagating through them if their frequency contents fall into the bandgaps, thus safeguarding the protected structures. Spring-mass models are commonly utilized to predict the wave propagation characteristics of local resonant metamaterials and metastructures. It is well understood that the formation of bandgaps is because of the generation of negative effective mass and negative effective stiffness owing to the out-of-phase local vibrations. However, in current literature, some studies derived the bandgaps associated with only the negative effective mass while others derived those from both the negative effective mass and negative effective stiffness. There has not been a systematic study and explanations on these differences, and there

[1] PhD Scholar. Email: hoangnhi.vo@postgrad.curtin.edu.au

[2] Senior Lecturer (Corresponding author). Email: thong.pham@curtin.edu.au

[3] John Curtin Distinguished Professor (Corresponding author). Email: hong.hao@curtin.edu.au

[4] Associate Professor. Email: Kaiming.bi@curtin.edu.au

[5] Associate Professor. Email: wensu.chen@curtin.edu.au

is also lack of understanding of the mechanics of bandgap formation, in particular the low-frequency bandgap. This paper presents a theoretical study to reinvestigate the formations of bandgaps in metaconcrete and meta-truss structure associated with the effective negative mass and stiffness, provides explanations of the discrepancies in the literature, and identifies the fundamental mechanism for the bandgap formation in metaconcrete and meta-truss structure. A comprehensive analysis is also provided for predicting bandgaps of metamaterials and metastructures, followed by a design procedure for engineering applications.

Keywords: Metaconcrete; Meta-truss bar; Bandgap; Fundamental mechanism; Negative effective mass; Negative effective stiffness.

1. Introduction

Blast/impact mitigations are of importance in engineering fields to prevent catastrophic consequences from terrorist activities and unexpected accidental explosions. For example, 2,996 people were killed in the 9/11 terrorist attack which caused a loss of US$135 billion [1], while an accidental explosion at Port of Beirut claimed 218 lives, 7,000 injuries and US$15 billion in property damage and left 300,000 people homeless [2]. Due to these escalating man-made hazards, the need for more robust protective systems is of vital importance [3-9]. As a topic of particular recent interest, metamaterials have attracted rapidly increasing attention due to their favourable wave mitigation capacity, as well as enormous potential for various practical applications. The concept of metamaterials was first discussed in 1968 [10] and is an interdisciplinary research topic that can be applied to numerous fields, e.g. mechanics, acoustics, optics, and electromagnetics, etc. Driven by the promising performance in the manipulation of vibrational energy, the metamaterials considered in this study have been regarded as candidates of enormous potential for many important applications in structural dynamics or vibration mitigation. Metamaterials are artificially engineered materials composed of internal structures that exhibit unusual physical properties in a specific range of excitation frequency [11-14], which could not be found in nature. These particular characteristics are triggered from the wave interference/out-of-phase motions of the internal components leading to negative effective properties. Accordingly, incident waves are filtered out, or in another word, they cannot propagate through metamaterials if their frequency contents fall into a certain range of frequencies, namely the “bandgap” [15, 16] or “attenuation band” [17, 18]. This characteristic of metamaterials has been widely adopted in many fields, including mechanical and manufacturing engineering as well as civil engineering.

Generally, metamaterials are based on two operating mechanisms to form a bandgap, i.e. Bragg scattering [19-23] and local resonance [21, 24-28]. The characteristics of the bandgap zones generated by these two mechanisms are completely different. While engineered materials with periodic features termed as phononic crystals have been utilized to form Bragg-scattering type of bandgap due to wave interference (Fig. 1a), the locally resonant bandgap is attributed to the out-of-phase motions of the resonators (Fig. 1b). The main limitation of phononic crystals stems from their dependence on the periodic spacing constant, which generates the high-frequency bandgap and thus is not suitable for low-frequency wave mitigations [15, 29, 30]. Conversely, the underlying mechanism of locally resonant metamaterial is the out-of-phase motions of the local resonators, which counteracts the applied excitation on the structures [31-35]. The bandgaps generated by the metamaterials associated with local resonance depend on the resonant frequency of the resonators embedded in the unit cell, thus making them suitable for low-frequency wave attenuation [36-39]. With this advantage, numerous local resonant metamaterials have been proposed and viewed as promising candidates for emerging applications, e.g. stress wave mitigation [26, 40], vibration suppression [18, 41-45], and seismic isolation [46-49].

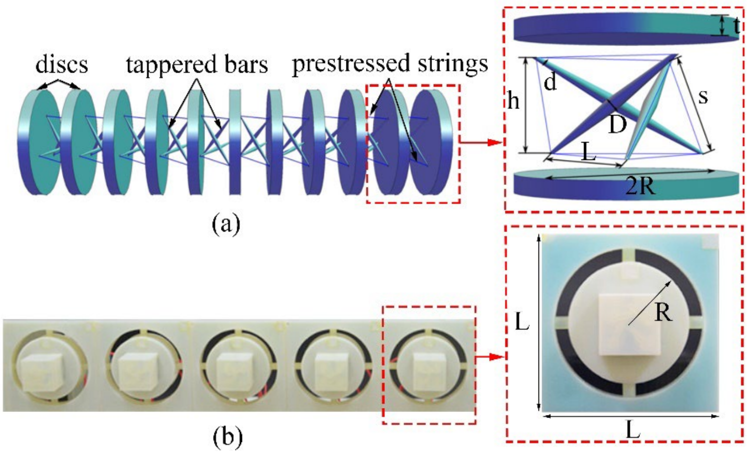

Fig. 1. Schematic view of metamaterials utilizing (a) Bragg scattering mechanism (e.g. Accordion-like meta-chain of circular discs interlayed by minimal tensegrity prisms, which

are formed by tapered bars and prestressed strings [50]) and (b) local resonant mechanism (e.g. tunable fluid-solid metamaterials [51]).

Many attempts have been reported using the spring-mass lattice system to examine the dynamic behaviours of metamaterials with local resonators. With their extraordinary effective characteristics, local resonant metamaterials/metastructures have demonstrated their effectiveness in many engineering applications. For example, a theoretical investigation on the bandgaps of the meta-beam was firstly proposed by Liu et al. [52] to study its effectiveness in vibration suppression while the negative mass and stiffness in the spring-mass structure were observed in an experimental study [53]. Tremendous efforts have also been made to enhance the wave attenuation of engineered concrete-like materials, i.e., metaconcrete which provides a promising solution for protecting concrete structures. Mitchell et al. [54] analytically and experimentally studied the effect of the design parameters on the performance of the metaconcrete. Subsequently, the influences of the geometries, dimensions, and material properties of resonant engineered aggregates on the prescribed bandgap region were numerically and experimentally investigated by Xu et al. [55-57]. Most of the previous studies on metamaterials or metastructures for structural protection are based on the spring-mass model for analytical derivations as shown in Fig. 2. However, the simplifications in establishing the spring-mass model in previous studies are not necessarily the same, which led to different predictions of bandgaps.

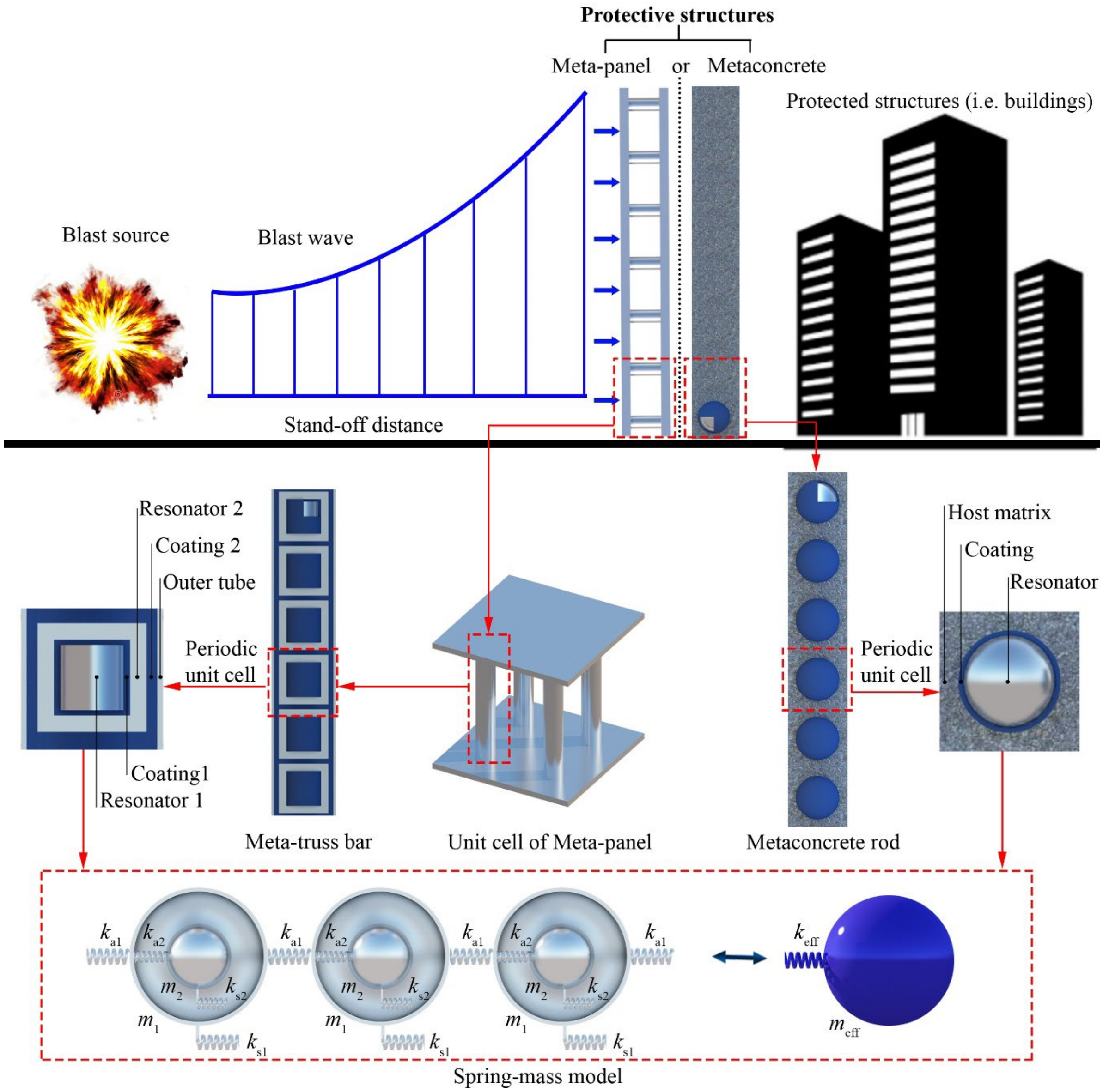

Fig. 2. Schematic view of the discrete spring-mass model adopted for metaconcrete and meta-truss bar in the meta-panel functioning as sacrificial cladding to protect the main structures from blast loading.

The generations of bandgaps in metamaterials and metastructures for stopping wave propagations depend on the negativity of the effective mass and stiffness. Besides, apart from solely considering the negative effective mass and negative effective stiffness, researchers have also considered the bandgap formation differently by substituting the negative effective stiffness by the negative effective modulus [58-63]. It should be noted that there is a reciprocal relationship between the negative effective stiffness and the negative effective modulus. In deriving the bandgaps of metamaterials and metastructures using the simplified spring-mass model, the parameters of the spring-mass model need to be properly determined, otherwise inaccurate bandgaps would be derived. There were a few spring-mass models proposed for metamaterials/metastructures, i.e. for metapanels [25, 26], metamaterials in acoustic field [64, 65], and metaconcrete [57, 66]. Theoretically, for a typical single degree of freedom (SDOF) spring-mass model, there should be two bandgaps when the negative effective mass and negative effective stiffness are induced. Some previous studies [24, 52] reported two bandgaps while the other studies [55, 67] only obtained one bandgap even though they all adopted the same type of spring-mass model. A detailed review found that this discrepancy is rooted in the existence of the negative effective stiffness because the former studies obtained both the negative effective mass and the negative effective stiffness while only the negative effective mass was obtained in the latter studies. This variation causes confusion and may lead to incorrect observations and understandings of the generations of bandgaps. Therefore, this study conducts theoretical derivations to reinvestigate the frequency bandgaps of metamaterials and metastructures based on the simplified spring-mass model. The results provide a thorough understanding of the frequency bandgap generations of metamaterials and metastructures, and also explain the differences in the previous studies. For complete understanding, three methods are utilized to determine the intrinsic bandgaps, including the effective properties (i.e. effective mass and effective stiffness), dispersion curves and transmission coefficient. These three methods are used to confirm the existence of bandgaps on preventing the wave propagations and crosscheck the outputs.

In addition, considering the fact that the frequency content of some popular engineering loading, e.g. earthquake excitation and mechanical vibration, is in low-frequency ranges (e.g.

0.5 – 25 Hz for earthquake loading [68]), tremendous efforts have been devoted to generating the bandgap associated with these low frequencies [68-70]. However, by using a similar spring-mass model, a few studies [24, 52] reported a bandgap in the low-frequency range starting from zero but this low-frequency bandgap is not reported in other studies [57, 67]. Vo et al. [24] found that the shear stiffness of the internal coating layer is responsible for widening the bandwidth of the low-frequency bandgap as observed in [52]. On the other hand, Jin et al. [67] analytically investigated the attenuation mechanism of metamaterials using the spring-mass model but did not observe the bandgap in the low-frequency range. The reason for this discrepancy is not systematically investigated and discussed.

As can be seen from the above review, two issues need to be clarified, i.e., (1) conditions to form two bandgaps in metaconcrete/meta-truss bar and (2) existence of low-frequency bandgap and the influences of the shear stiffness on the bandgaps. This paper presents theoretical derivations, supported by experimental and numerical results to examine the mechanisms behind these two issues and provides explanations on why different observations on bandgaps were reported in the previous studies. The results in this study foster appropriate design for practical applications of metaconcrete and meta-truss bar. A detailed design procedure of the meta-truss bar for resisting the targeted impulsive loads, especially in the low-frequency range is given as an application example.

2. Analytical model

As mentioned previously, the concept of metamaterials or metastructures has been adopted in numerous engineering applications, e.g. metaconcrete, metabeam, and metapanel. The simplified spring-mass models are often utilized for analysis. In this study, a spring-mass model for a metaconcrete rod and a meta-truss bar is chosen as an example, as shown in Fig. 2. It should be noted that the considered metaconcrete rod is a periodic structure consisting of a finite number of metaconcrete unit cells, and in which, normal aggregates of conventional concrete embedded in the host matrix are replaced by spherical resonators comprising a heavy metal core coated with a soft outer layer; and the configuration of the meta-truss bar is a cylindrical hollow tube containing dual resonators suspended by soft coatings in a periodic arrangement.

2.1 Spring-mass model for metaconcrete rod

2.1.1 Conventional analysis

A discrete spring-mass lattice system containing infinite structural components (called unit cells) that are connected together end-to-end to represent the metaconcrete rod is illustrated in Fig. 3. In the model, the external mass (i.e. host matrix) is denoted by m_1 while the internal mass (i.e. resonator) and the stiffness of the axial spring connecting the two adjacent outer masses are denoted by m_2 and k_{a1}, respectively. The internal mass is an oscillator whose displacement counteracts that of the external mass when the local resonant phenomenon occurs. The stiffness of the axial spring connecting the oscillator and the external mass is denoted by k_{a2}. It should be noted that the shear stiffness k_{s1} and k_{s2} in Fig. 2 are equal to zero in this conceptualized model, as in previous studies [55, 56]. The influence of neglecting the shear stiffness will be discussed later.

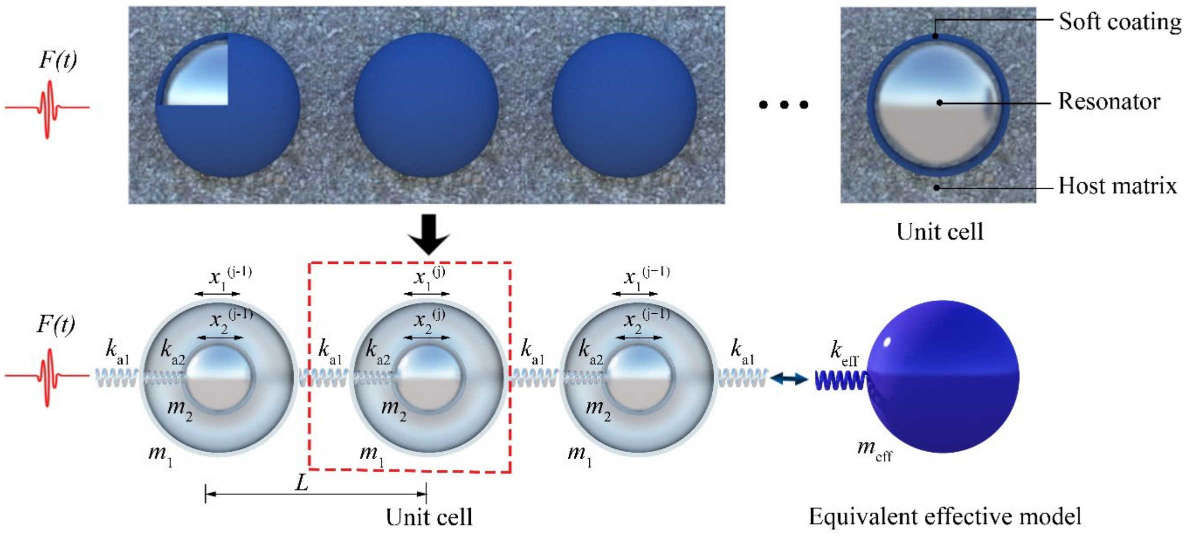

Fig. 3. Schematic view of the simplified spring-mass model for metaconcrete, including external mass m_1, internal mass m_2, external axial stiffness k_{a1} and internal axial stiffness k_{a2} with respect to the continuum media and its equivalent effective model with effective mass m_{eff} and effective stiffness k_{eff}.

To discuss the kinematic modelling of this system, the free vibration equation of motion of the external mass for the j^{th} unit cell can be expressed as Eq. (1):

$$m_1\ddot{x}_1^{(j)} + k_{a1}\left(2x_1^{(j)} - x_1^{(j+1)} - x_1^{(j-1)}\right) + k_{a2}\left(x_1^{(j)} - x_2^{(j)}\right) = 0 \tag{1}$$

where the overdot denotes the derivative with respect to time t while x_1 and x_2 are respectively the displacements of the external and internal masses in the j^{th} unit cell.

The dynamic equilibrium equation for the internal mass of the unit cell j is

$$m_2\ddot{x}_2^{(j)} + k_{a2}\left(x_2^{(j)} - x_1^{(j)}\right) = 0 \tag{2}$$

Rewrite Eqs. (1) and (2) in the matrix form, it has

$$\begin{bmatrix} m_1 & 0 \\ 0 & m_2 \end{bmatrix}\begin{bmatrix} \ddot{x}_1^{(j)} \\ \ddot{x}_2^{(j)} \end{bmatrix} + \begin{bmatrix} 2k_{a1}+k_{a2} & -k_{a2} \\ -k_{a2} & k_{a2} \end{bmatrix}\begin{bmatrix} x_1^{(j)} \\ x_2^{(j)} \end{bmatrix} - \begin{bmatrix} k_{a1}\left(x_1^{(j+1)} + x_1^{(j-1)}\right) \\ 0 \end{bmatrix} = \begin{bmatrix} 0 \\ 0 \end{bmatrix} \tag{3}$$

The harmonic wave solution for the displacement of the j^{th} unit cell is given as Eq. (4) based on Bloch's theorem. This theory was developed to solve differential Schrodinger equations in mathematics and physics.

$$x^{(j)} = Xe^{i(jqL-\omega t)} \tag{4}$$

$$x^{(j+1)} = Xe^{i(jqL-\omega t)}e^{iqL}$$

$$x^{(j-1)} = Xe^{i(jqL-\omega t)}e^{-iqL}$$

where L is the length of the unit cell, q is the wavenumber, ω is the angular frequency, i is the imaginary unit, and X is the displacement amplitude.

The lattice system consisting of spring-mass unit cells is considered as an equivalent solid object and substituting Eq. (4) into Eq. (3) results in an eigenvalue problem of the form $\left[\mathbf{K}(q)-\mathbf{M}\omega^2\right]\mathbf{u}=0$. Solving this eigen function, the vibration frequencies can be obtained and the effective mass (m_{eff}) of the unit cell is derived as [67, 71]

$$m_{eff} = m_1 + \frac{m_2\omega_0^2}{\omega_0^2-\omega^2}, \tag{5}$$

where the natural vibration frequency of the unit cell is $\omega_0^2 = \dfrac{k_{a2}}{m_2}$

As shown, the effective mass depends not only on the physical masses m_1 and m_2, but also on the natural vibration frequency of the unit cell ω_0 and the excitation frequency ω. When the excitation frequency is larger than the natural vibration frequency of the unit cell, the effective mass could become negative. The underlying goal for developing the effective properties of this model is to establish the relationship between the frequency of the incident excitation and the locally resonant frequency of the unit cell. As shown in Eq. (5), the effective mass significantly changes when the incident frequency approaches the natural vibration frequency of the resonator and can become negative, leading to the favourable wave attenuation characteristics of the meta-system. When the effective mass (m_{eff}) becomes negative, the motions of m_1 and m_2 are out-of-phase, which implies that the mechanical wave of this frequency range cannot pass through the system. The wave energy is transferred to local vibrations of unit cells and cancelled by one another due to out-of-phase motions instead of propagating through the system. As a result, the wave energy with frequency coincident with the bandgaps is greatly attenuated.

The physical meaning and mechanism of metamaterials associated with the negative effective mass on attenuating wave propagation have been documented in the previous studies [55, 57]. However, one major limitation of the conventional approach is that it only considers the effective mass negativity which exists in a very narrow bandgap region, specifically near the natural vibration frequency of the internal mass. This approach has been widely adopted by other studies for metaconcrete [57, 66]. Considering only the negative effective mass cannot predict the bandgap in the high-frequency range either as observed in the experimental tests reported by Mitchell et al. [72] as shown in Fig. 4, in which a metaconcrete rod is similar to the one illustrated in Fig. 3 was tested. In other words, only considering negative effective mass failed to capture the actual behaviours of metaconcrete since the experimental results exhibited two bandgaps while the analytical prediction gave only one narrow bandgap.

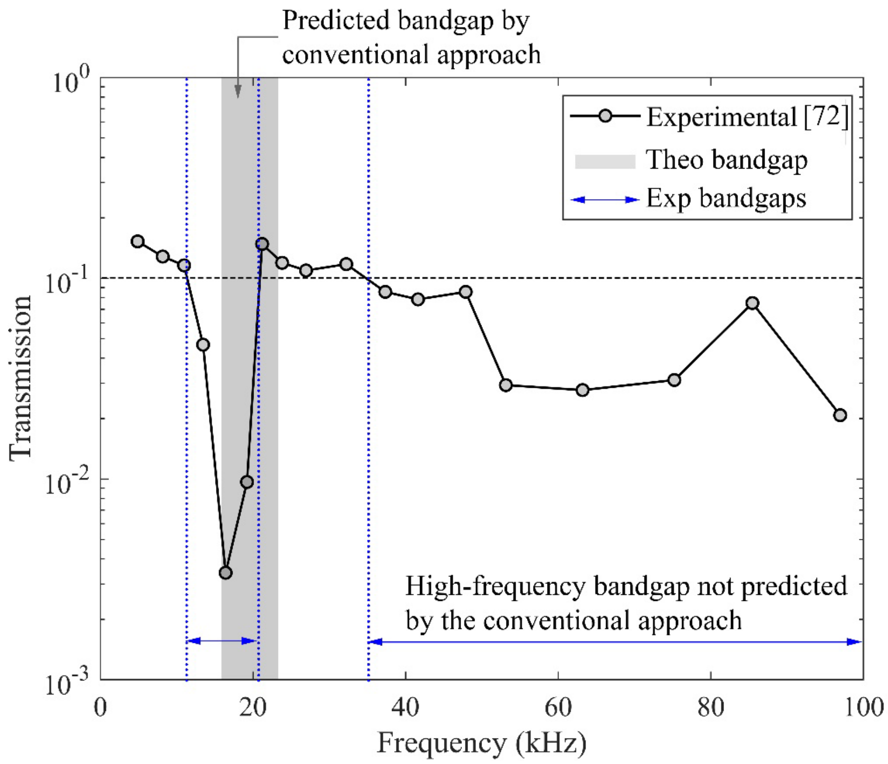

Fig. 4. Experimental transmission coefficient of the metaconcrete exhibits a high-frequency bandgap not predicted by the conventional approach. Note: the transmission coefficient presented is given by the ratio of the amount of energy transmitted to the last unit to the total energy of the system. (For interpretation of the references to colour in this figure legend, readers are referred to the web version of this article).

2.1.2 Comprehensive analysis

In response to the limitations of the conventional analysis and to gain an insightful understanding of the underlying physics of the negative effective properties based on the analysis of the spring-mass model, a comprehensive derivation and discussion are presented in this section. This comprehensive derivation includes both the effective mass and the effective stiffness. The system containing an infinite number of periodically-arranged spring-mass in Fig. 3 is adopted in this section to study its frequency-dependent wave phenomenon. For double verification of the determined bandgaps from the spring-mass model, three methods including the effective properties, wave dispersive analysis and wave transmission are used in this study.

2.1.2.1 Identification of the effective parameters

The effective mass and the effective stiffness are the most important parameters of the spring-mass model. In general, bandgaps are formed when these effective parameters become negative. As discussed above, the effective mass is given by Eq. (5) while the effective stiffness is neglected in some previous studies [56, 57]. In this subsection, the formula of the negative stiffness is derived to investigate its reciprocal relationship with the bandgaps. To define the effective stiffness from the lumped mass model, the unit cell is assumed as homogeneous and can be calculated as follows [52]:

$$k_{eff} = k_{a1} + \frac{1}{4}k_{a2} - \frac{1}{4}\left(m_1\omega^2 + \frac{k_{a2}\omega_0^2}{\omega_0^2 - \omega^2}\right),\ \omega_0^2 = \frac{k_{a2}}{m_2} \tag{6}$$

From Eq. (6), it is obvious that depending on the stiffness, mass and natural vibration frequency, the effective stiffness could also be negative, resulting in favourable bandgaps. The conventional analysis which only considered the effective mass has overlooked this bandgap in its prediction. This study provides a comprehensive analysis of bandgap formation considering both the effective mass and the effective stiffness. The bandgaps obtained from the negative effective properties are cross-checked with other methods, which will be derived in the following sections.

2.1.2.2 Wave dispersive analysis

In addition to the direct derivation, wave dispersive analysis can be also adopted to determine bandgaps. Dispersion curves provide information on whether or not a wave could propagate through the system at certain frequency ranges. It can be used to determine the frequency stop-bands (bandgaps) wherein the wave vector is imaginary, therefore, the plane waves experience rapid attenuation. To derive the dispersion curves, the solutions of the harmonic wave of the j^{th},

$(j+1)^{\text{th}}$, $(j-1)^{\text{th}}$ unit cells in Eq. (4) are adopted, and their derivative functions can be obtained as follows:

$$\ddot{x}^{(j)} = -\omega^2 X e^{i(jqL-\omega t)} = -\omega^2 x^{(j)} \tag{7}$$

$$\ddot{x}^{(j+1)} = -\omega^2 X e^{i(jqL-\omega t)} e^{iqL} = -\omega^2 x^{(j)} e^{iqL}$$

$$x^{(j-1)} = -\omega^2 X e^{i(jqL-\omega t)} e^{-iqL} = -\omega^2 x^{(j)} e^{-iqL}$$

Substituting Eq. (7) into Eq. (3), the dynamic equilibrium equation can be rewritten as:

$$\begin{bmatrix} -\omega^2 m_1 & 0 \\ 0 & -\omega^2 m_2 \end{bmatrix} \begin{bmatrix} x_1^{(j)} \\ x_2^{(j)} \end{bmatrix} + \begin{bmatrix} 2k_{a1}+k_{a2} & -k_{a2} \\ -k_{a2} & k_{a2} \end{bmatrix} \begin{bmatrix} x_1^{(j)} \\ x_2^{(j)} \end{bmatrix} - \begin{bmatrix} k_{a1}\left(e^{iqL}+e^{-iqL}\right)x_1^{(j)} \\ 0 \end{bmatrix} = \begin{bmatrix} 0 \\ 0 \end{bmatrix} \tag{8}$$

By applying the identity $e^{iqL}+e^{-iqL} = 2\cos\left(qL\right)$, Eq. (8) becomes:

$$\begin{bmatrix} -\omega^2 m_1 & 0 \\ 0 & -\omega^2 m_2 \end{bmatrix} \begin{bmatrix} x_1^{(j)} \\ x_2^{(j)} \end{bmatrix} + \begin{bmatrix} 2k_{a1}+k_{a2} & -k_{a2} \\ -k_{a2} & k_{a2} \end{bmatrix} \begin{bmatrix} x_1^{(j)} \\ x_2^{(j)} \end{bmatrix} - \begin{bmatrix} 2k_{a1}\cos\left(qL\right)x_1^{(j)} \\ 0 \end{bmatrix} = \begin{bmatrix} 0 \\ 0 \end{bmatrix} \tag{9}$$

Solving Eq. (9), one obtains the relation between the wave number *q* and the angular frequency *ω*, which is called the wave dispersion relation.

$$-m_1\omega^2 x_1^{(j)} + 2k_{a1}\left(1-\cos\left(qL\right)\right)x_1^{(j)} + k_{a2}\left(1-\frac{k_{a2}}{k_{a2}-m_2\omega^2}\right)x_1^{(j)} = 0 \tag{10}$$

The frequency gap between the wave dispersion curves is called the bandgap, which means there is no positive real solution for *ω* with the change of *q* in the bandgap frequency range. In these excitation frequency ranges, only exponentially decaying solutions exist.

Eq. (10) can be further rearranged as

$$\cos qL = 1 - \frac{m_1\omega^2 - k_{a2}\left(1-\dfrac{\omega_0^2}{\omega_0^2-\omega^2}\right)}{2k_{a1}}, \quad \omega_0^2 = \frac{k_{a2}}{m_2} \tag{11}$$

2.1.2.3 Wave transmission

Wave transmission analysis can also be used to determine the bandgaps. The wave transmission coefficient of the spring-mass model, defined as the ratio between the displacements of the output signal to the input excitation, can be calculated as:

$$T = \left| \prod_{j=1}^{N} T^{(j)} \right| = \left| \prod_{j=1}^{N} \frac{x^{(j)}}{x^{(j-1)}} \right| \tag{12}$$

where $x^{(j)}$ is the displacement of the j^{th} unit cell, and N is the total number of the unit cells.

Rearrange Eq. (11) as

$$\omega^2 = 2\frac{k_{a1}}{m_{eff}}\left(1-\cos\left(qL\right)\right) \tag{13}$$

and substituting $e^{iqL} + e^{-iqL} = 2\cos\left(qL\right)$, from Eq. (9) it has

$$\left(2k_1 - m_{eff}\omega^2\right)x^{(j)} = k_{a1}\left(x^{(j+1)} + x^{(j-1)}\right),\ j = 1,2,...,N-1 \tag{14}$$

$$\left(k_{a1} - m_{eff}\omega^2\right)x^{(j)} = k_{a1}x^{(j-1)},\ j = N$$

By substituting the above equation into Eq. (12), the wave transmission coefficient can be formulated as follows:

$$T^{(j)} = \frac{k_{a1}}{k_{a1}\left(2-T^{(j+1)}\right) - m_{eff}\omega^2},\ j = 1,2,...,N-1 \tag{15}$$

$$T^{(N)} = \frac{k_{a1}}{k_{a1} - m_{eff}\omega^2},\ j = N$$

where $T^{(j)}$ is the transmission coefficient of the j^{th} unit cell, and N is the total number of the unit cells.

2.2 Spring-mass model for meta-truss bar (considering the shear stiffness of the coating layers)

It was mentioned previously that the metaconcrete and meta-truss bar adopted a similar concept but their characteristics are slightly different. The cores in the metaconcrete are usually spherical while the core in the meta-truss bar is often cylindrical. Accordingly, the shear stiffness between the core and the mortar matrix in metaconcrete with spherical units is minimum owing to the point contact, but the shear resistance between the matrix and the cylindrical core in the meta-truss bar is considerable owing to the surface contact, therefore needs to be considered in the spring-mass model. The analytical analysis in this study shows this shear stiffness governs the low-frequency bandgap.

To investigate the wave propagation in the meta-truss bar, especially in the low-frequency range, an equivalent spring-mass system with the shear spring stiffness of a continuum unit cell is proposed and illustrated in Fig. 5. It should be noted that, to straightforwardly compare the bandgap mechanism between this model (i.e. the model considering the shear stiffness) and the model adopted for metaconcrete without considering the shear stiffness, the meta-truss bar in Fig. 5 is selected as a representative. Besides the axial spring stiffnesses k_{a1} and k_{a2} respectively connecting the external mass with its adjacent unit cell and with the internal mass, this model considers the two shear spring stiffnesses, i.e. k_{s1} and k_{s2}.

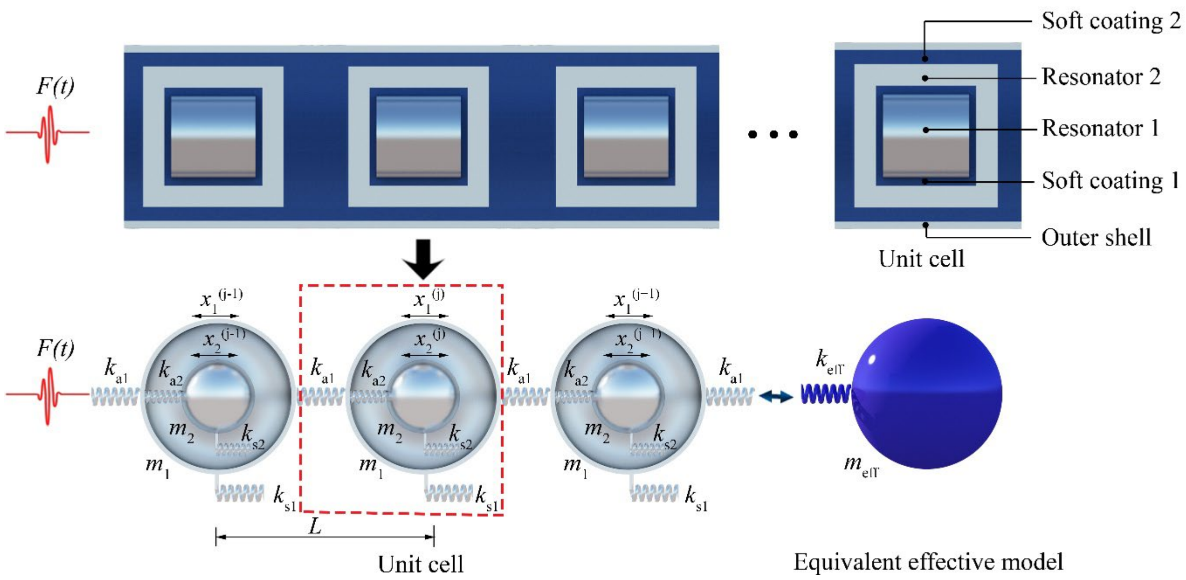

Fig. 5. Schematic view of the simplified spring-mass model for meta-truss bar, including external mass m_1, internal mass m_2, external axial stiffness k_{a1}, internal axial stiffness k_{a2}, external shear stiffness k_{s1}, and internal shear stiffness k_{s2} with respect to the continuum media and its equivalent effective model with effective mass m_{eff} and effective stiffness k_{eff}.

Using the analytical model established in Fig. 4, one can derive the equations of motion of the unit cell j^{th} as

$$m_1\ddot{x}_1^{(j)} + k_{a1}\left(2x_1^{(j)} - x_1^{(j+1)} - x_1^{(j-1)}\right) + k_{a2}\left(x_1^{(j)} - x_2^{(j)}\right) + k_{s1}x_1^{(j)} = 0 \quad (16)$$

$$m_2\ddot{x}_2^{(j)} + k_{a2}\left(x_2^{(j)} - x_1^{(j)}\right) + k_{s2}x_2^{(j)} = 0$$

Rewrite Eqs. (16) into a matrix

$$\begin{bmatrix} m_1 & 0 \\ 0 & m_2 \end{bmatrix}\begin{bmatrix} \ddot{x}_1^{(j)} \\ \ddot{x}_2^{(j)} \end{bmatrix} + \begin{bmatrix} 2k_{a1} + k_{a2} + k_{s1} & -k_{a2} \\ -k_{a2} & k_{a2} + k_{s2} \end{bmatrix}\begin{bmatrix} x_1^{(j)} \\ x_2^{(j)} \end{bmatrix} - \begin{bmatrix} k_{a1}\left(x_1^{(j+1)} + x_1^{(j-1)}\right) \\ 0 \end{bmatrix} = \begin{bmatrix} 0 \\ 0 \end{bmatrix} \quad (17)$$

Similar approaches are utilized to determine the effective parameters. The effective mass and the effective stiffness of the system are derived as [24]

$$m_{eff} = m_1 + \left[\frac{k_{a2}^2 / \left(k_{a2} + k_{s2}\right)}{\omega_0^2 - \omega^2} - \left(k_{s1} + k_{a2}\right)\right]\frac{1}{\omega^2} \quad (18)$$

$$k_{eff} = k_1 + \frac{1}{4}\left(k_{s1} + k_{a2}\right) - \frac{1}{4}\left(m_1\omega^2 + \frac{k_{a2}^2 / \left(k_{a2} + k_{s2}\right)}{\omega_0^2 - \omega^2}\right)$$

where the natural vibration frequency is defined by $\omega_0^2 = \frac{k_{a2} + k_{s2}}{m_2}$.

Based on the Bloch-Floquet theory, in which the motion must satisfy the Bloch periodicity condition, the dispersion relation can be obtained as

$$\cos qL = 1 - \frac{m_1\omega^2 - \left(k_{s1} + k_{a2}\right) + \dfrac{k_{a2}^2 / \left(k_{a2} + k_{s2}\right)}{\omega_0^2 - \omega^2}}{2k_{a1}} \quad (19)$$

Using the transmission equations of the starting and ending unit cells, the displacement transmission coefficient of the entire system can be expressed as

$$T = \left| \prod_{j=1}^{N} T^{(j)} \right| = \left| \prod_{j=1}^{N} \frac{x^{(j)}}{x^{(j-1)}} \right| \tag{20}$$

where $T^{(j)} = \dfrac{k_{a1}}{k_{a1}\left(2 - T^{(j+1)}\right) - m_{eff}\omega^2}$ with $j = 1, ..., N-1$, and $T^{(N)} = \dfrac{k_{a1}}{k_{a1} - m_{eff}\omega^2}$

3. Verification and discussion of mechanisms for bandgap generation

In this section, the spring-mass models used to predict the bandgaps of metaconcrete and meta-truss bar are verified and discussed. From the above analytical derivations, it is expected that the metaconcrete has two bandgaps while the meta-truss bar has one additional bandgap in the low-frequency range due to the contribution of the shear stiffness. For validation, the experimental data from the previous study [72] and the numerical results are utilized to verify the analytical models.

3.1 Spring-mass model for predicting bandgaps of metaconcrete

A number of experimental tests reported in the literature, e.g., results shown in Fig. 4 from [72] illustrate that metaconcrete structure has two bandgaps although many studies overlooked the second bandgap and the discussions concentrated mainly on the first bandgap associated with the negative effective mass. This section analytically demonstrates metaconcrete has two bandgaps and presents methodologies on how to determine them. The periodic metaconcrete rod (shown in Fig. 6) consists of three components, including the matrix (mortar), soft coating (nylon) and spherical inclusion (lead). Each part within the model is assigned with the appropriate properties as given in Table 1, where v denotes Poisson's ratio, while ρ and E respectively represent the density and elastic modulus. Details of the considered structure have been reported in previous study, which is therefore not repeated herein for brevity. According to the previous explanation, the considered metaconcrete rod is conceptualized as a spring-mass model.

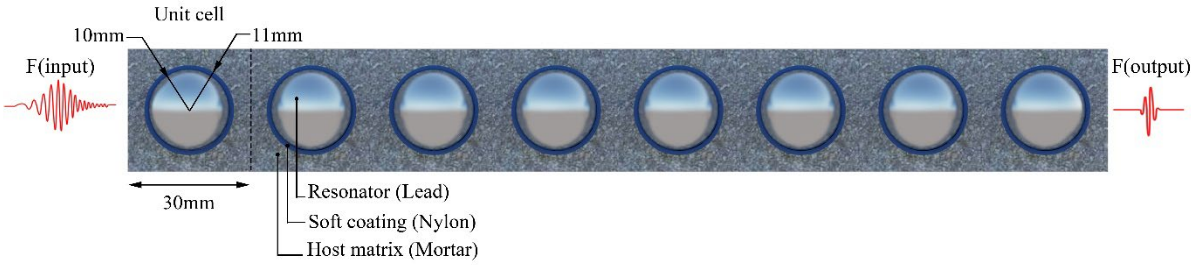

Fig. 6. Schematic view of a metaconcrete rod used for modal analysis consisting of 8 unit cells in which each unit cells comprises of the matrix (mortar), the soft coating (nylon) and the spherical inclusion (lead).

Table 1. Elastic material properties for all components.

Materials	Mortar	Lead	Nylon
ρ (kg/m^3)	2,500	11,400	1150
E (GPa)	30	16	1
v	0.2	0.44	0.4

To reveal the true relationship between the effective parameters and the bandgaps in the frequency band structure, the formations of the effective mass and effective stiffness are derived in Section 2 using the Floquet-Bloch theory. The effective mass and effective stiffness of the considered model are examined in detail, which will be used as the foundation for the explanation of the bandgap formation in the system. Fig. 7 shows the effective mass and effective stiffness of the considered model calculated analytically over the frequencies of interest. As expected, the effective mass of the model becomes negative at a narrow frequency band from 17.5 kHz to 26.4 kHz (blue-shaded area), due to the out-of-phase motions of the resonator and the host matrix. It is worth mentioning that the wave manipulation capacity is significantly influenced by the local resonance of the resonator which is defined in Eq. (5) by $\omega_0 = \sqrt{k_{a2} / m_2} = 17.5\,\text{kHz}$.

Fig. 6 shows that considering the effective mass for determination of the attenuation band can only predict a portion of the first bandgap (blue-shaded area, [17.5 – 26.4]), i.e., under-predicts the first bandgap width. The first bandgap actually consists of the blue-shaded area caused by negative effective mass and the red-shaded area induced by negative effective stiffness, i.e. [13.5 – 17.5] kHz. Fig. 7 shows a second bandgap in the red-shaded area, i.e. [> 35.9] kHz, also due to the negative effective stiffness. As illustrated, when the vibration frequency approaches the resonant frequency, the effective stiffness dramatically decreases to negative values in a narrow frequency region, then jumps to high positive values after passing the resonant frequency. Afterwards, the effective stiffness returns rapidly to zero before becoming negative again when vibration frequency is large. The mechanism for forming a portion of the 1st bandgap of the effective stiffness is attributed to its negative values when approaching the local resonant frequency of the resonator, and its 2nd bandgap is generated when vibration frequency is large that leads the effective stiffness to a negative value. This result can explain the high-frequency bandgap of the considered model as observed in the tests.

By combining the results in Fig. 7, two observations can be found. Firstly, there are two bandgaps induced by both the effective mass and effective stiffness, which is different from previous studies on metaconcrete where only one bandgap was reported. Secondly, the first bandgap consists of two portions induced by the negative effective mass and negative effective stiffness. Accordingly, the width of the first bandgap should be wider than the case when only the effective mass is considered as in previous studies [57, 66].

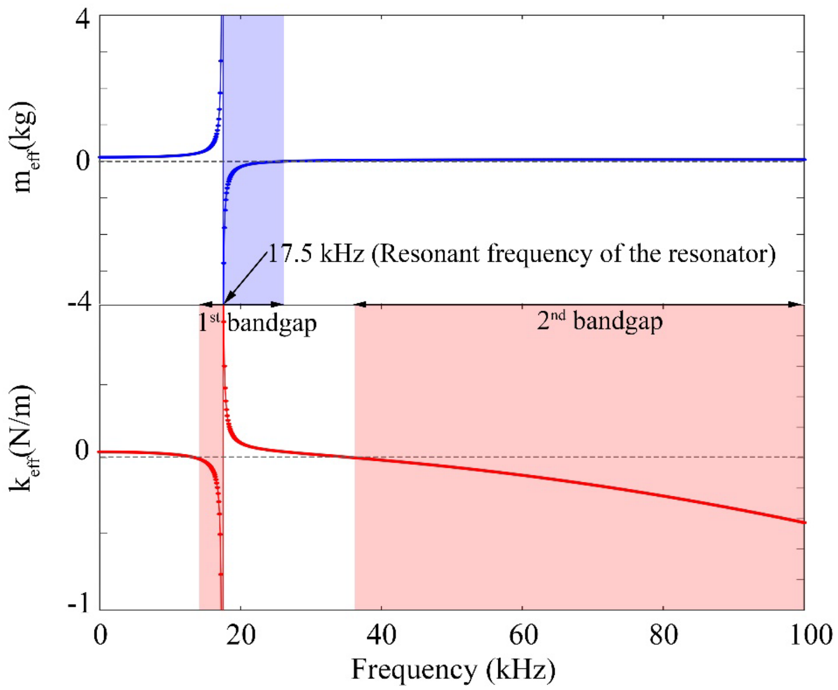

Fig. 7. Effective parameters of the spring-mass model to show the theoretical bandgap regions of metaconcrete including the effective mass on the upper side and the effective stiffness on the lower side. Shaded areas in blue and red indicate the bandgaps associated with the negativity of the effective mass and effective stiffness, respectively (For interpretation of the references to colour in this figure legend, readers are referred to the web version of this article).

To further elaborate the mechanism of the considered model and verify the frequency band structure given by the effective properties, the real and imaginary parts of the dispersion curves produced by using the periodic spring-mass model are illustrated in Fig. 8. The blue line in the figure denotes the real part while the corresponding imaginary part is represented by the red line. As shown, the imaginary part of the wavenumber in the complex frequency band is not equal to zero [$\mathrm{Im}(qL) \neq 0$] at the two regions of frequencies (shaded areas), indicating complete bandgap frequency regions. In other words, the frequency band structure of this model exhibits two bandgaps [$\mathrm{Re}(qL)=0$] and two passbands [$\mathrm{Re}(qL) \neq 0$].

It is clear that the bandgaps in Fig. 8 match well with the frequency bandgaps derived above based on the negative effective mass and stiffness, i.e., the first bandgap from 13.5 kHz to 26.4 kHz and over 35.9 kHz for the 2nd bandgap. These results indicate that once the effective properties become negative, the corresponding wavenumber would become complex, resulting in wave attenuation and eventually preventing wave transmitting through the system.

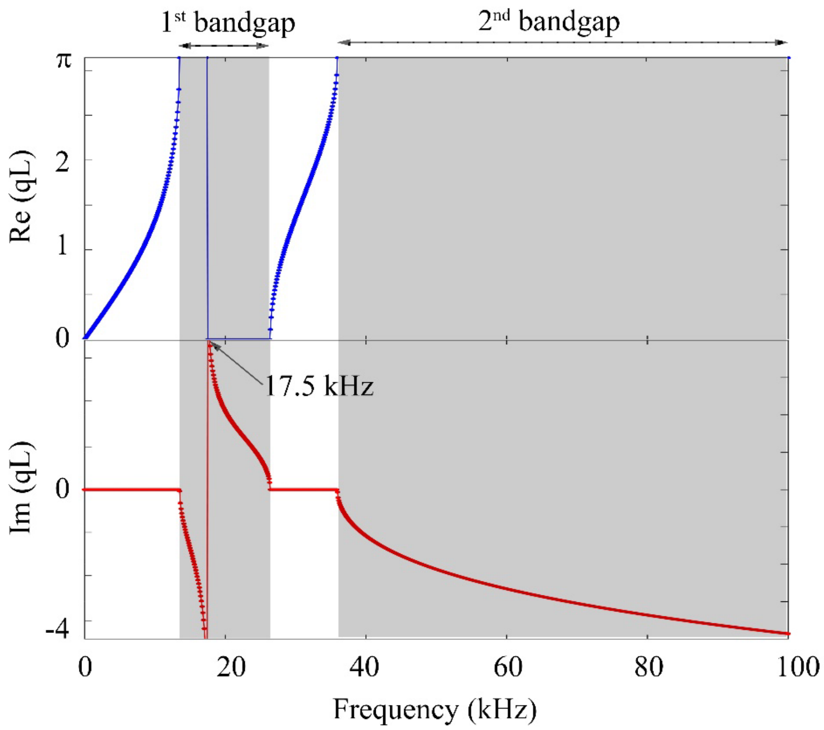

Fig. 8. Complex frequency band structure of the dispersion curves of the spring-mass model to show the theoretical bandgap regions of metaconcrete including the real part on the upper side and the imaginary part on the lower side. Shaded areas in grey indicate the bandgaps (For interpretation of the references to colour in this figure legend, readers are referred to the web version of this article).

In addition to the wave dispersion curves, the wave transmission can also be utilized to study the mitigation characteristics of wave propagation in metaconcrete. As shown in Fig. 9, the low transmission of the system is observed in the frequency ranges coincident with the negative effective properties in Fig. 7. These observations demonstrate that both methods yield the same results. To further validate the bandgaps obtained in the above derivations, the tunable wave transmission coefficients from the experimental results and those obtained above, as well as the bandgaps derived by considering only the negative effective mass are compared in Fig. 9. As shown, the experimental results also gave two bandgaps as denoted by grey-shaded areas. The bandgap associated with the negative effective mass (i.e. conventional analysis) represented by the red-shaded area only captures a portion of the 1st bandgap of the experimental result (grey-shaded area), demonstrating again that considering the negative effective mass alone is insufficient to obtain the complete bandgaps of metaconcrete.

Meanwhile, the combined bandgaps associated with both the negative effective mass and negative effective stiffness match well with the experimental results (Fig. 9), which confirms the validity of the above analysis and the need for considering the negative effective stiffness in deriving the bandgaps. In particular, a sharp wave transmission dipping at 17.5 kHz is found in both the analytical derivation and experimental test, which is caused by the local resonance of the resonator. The bandgaps due to the local resonator obtained from the analytical derivation agree well with those observed in the experimental tests. In the experimental tests, the obtained frequency bandgaps are from 12.5 kHz to 23.5 kHz and >34.5 kHz, respectively for the 1st and the 2nd bandgap while the corresponding ranges from the analytical derivation are 13.5 kHz to 26.4 kHz and >35.9 kHz. It should be noted that there are some slight variations between the experimental result and the theoretical results. This is because, as discussed above, in theoretical derivation the model is assumed to be homogeneous with idealized material properties, and an infinite number of unit cells connected by springs, i.e., no boundary reflection, while the tested specimen in the experiment has a finite length with only 8 unit cells and the specimen material properties are inhomogeneous.

Besides, as observed from the experiment in Fig. 9, the transmission coefficients in the low-frequency bandgap are smaller than those in the high-frequency bandgap. It is attributed to the fact that the number of unit cells in the considered structure has a significant effect on the high-frequency bandgap while it has limited influence on the low-frequency bandgap, which is in close proximity of the local resonant frequency (i.e. 17.5 kHz). Specifically, as proven in the previous study [72], when increasing the number of unit cells from 8 units to 36 units, the transmission coefficients in the low-frequency bandgap is unchanged while those of the high-frequency bandgap decrease to a converged value.

The above results indicate that both the effective mass and effective stiffness need to be considered in deriving the frequency bandgaps. The analytical results agree well with those observed in the experimental tests.

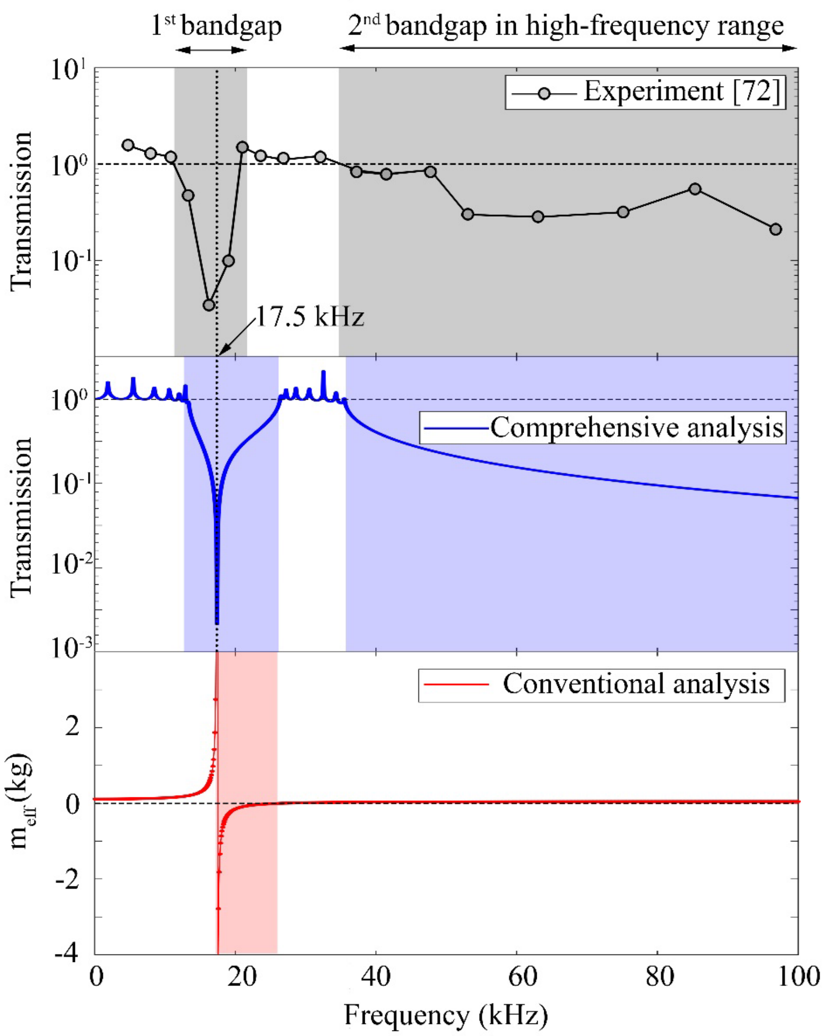

Fig. 9. Bandgaps obtained from experimental test, prediction considering both the effective mass and effective stiffness, and prediction considering only the effective mass. Shaded areas in blue and red indicate the bandgaps associated with the comprehensive analysis and conventional analysis, respectively while the bandgaps from the experiment are denoted by the grey-shaded area (For interpretation of the references to colour in this figure legend, readers are referred to the web version of this article).

3.2 Spring-mass model for predicting bandgaps of meta-truss bar

Section 3.1 discusses a spring-mass model for metaconcrete which ignores the shear behaviour between the resonators and the host matrix. The shear stiffness can be ignored because of the spherical shape of the unit cells in metaconcrete which results in minimum shear resistance between the unit cells and the matrix. For a meta-truss bar, however, the unit cell usually has cylindrical shapes for easy implementation as studied in [25, 26]. When simplifying the meta-truss bar to the spring-mass model, the shear resistance between the resonators and the matrix cannot be ignored because of the large shear area of the cylindrical surface. Without loss of generality, the meta-truss bar (Fig. 10) consists of eight periodical unit cells, in which each unit cell comprises five components including the outer shell, soft coatings, and resonators. For brevity, details of the meta-truss bar are not presented herein but can refer to a previous study by Vo et al. [25]. The material properties are summarized in Table 2.

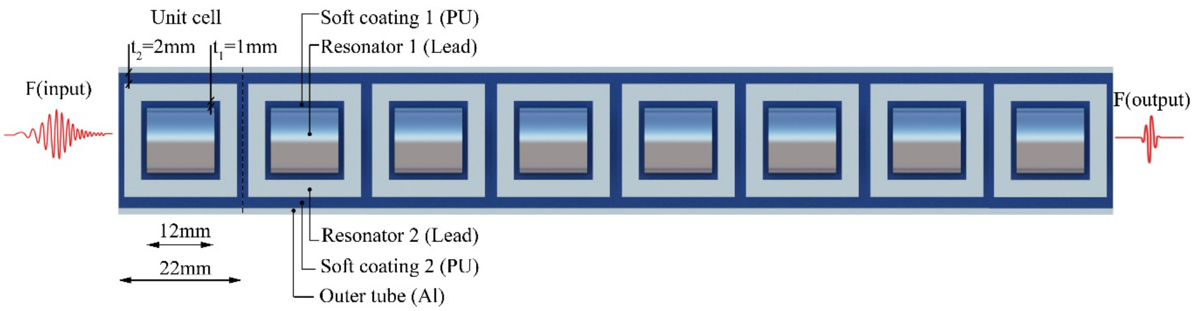

Fig. 10. Schematic view of the meta-truss bar used for modal analysis consisting of 8 unit cells in which each unit cells comprises of the outer shell (Al), two soft coatings (PU) and the two resonators (Al).

Table 2. Elastic material properties for all components of the meta-truss bar [25].

Materials	Aluminium	Polyurethane	Lead
ρ (kg/m^3)	2,770	900	11,400
E (GPa)	70	0.147	16
ν	0.33	0.42	0.44

From the derivations presented in Eq. (18), the analytical formulae for the effective mass and effective stiffness with respect to the vibration frequency can be straightforwardly determined.

Fig. 11 shows the effective mass and effective stiffness of the meta-truss bar, in which the bandgaps correspond to their negative values. The blue-shaded regions represent the frequency ranges of the bandgaps related to the negative effective mass while those associated with the negative effective stiffness are marked by red-shaded areas. It is observed again that the bandgap at the local resonant frequency does not start at the natural frequency of the local resonator (i.e. 10.3 kHz), but at a lower frequency because of the contribution of the negative stiffness. The bandgap close to the local resonant frequency is in the range of 9.3 kHz to 11.5 kHz. Combining both the effective parameters, it is found that there are three bandgaps in this considered meta-truss bar. Particularly, two bandgaps in the low and high-frequency regions are independent of each other and are formed because of the negative effective mass and negative effective stiffness, respectively, while the bandgap in the middle is the combination of the negativity of the effective mass and effective stiffness. Compared to the frequency band structure in Fig. 7, the second (middle range) and the third (high-frequency range) bandgaps are similar as discussed above in metaconcrete, while the metaconcrete considered above does not have the first (low-frequency range) bandgap associated with the negative effective mass. This is because of the shear stiffness between the matrix and the unit cell in the meta-truss bar that generates this low-frequency bandgap from 0 – 5 kHz. This low-frequency bandgap is of great importance in the field of engineering applications, e.g. vibration control, seismic isolation, and mechanical harness because loading frequencies are mainly in the low-frequency range. This finding is of foremost importance since it reveals how the mechanism can be fully leveraged to achieve a wider range of the bandgap frequencies for which wave propagation is reduced, especially in a low-frequency range.

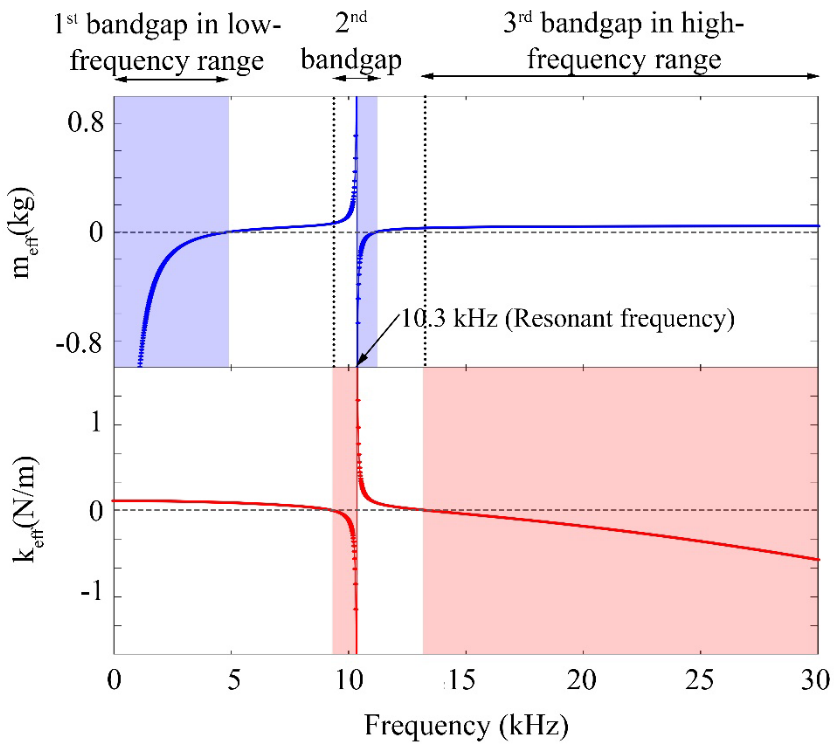

Fig. 11. Effective parameters of the spring-mass model with shear stiffness to show the theoretical bandgap regions of metaconcrete including the effective mass on the upper side and the effective stiffness on the lower side. Shaded areas in blue and red indicate the bandgaps associated with the negativity of the effective mass and effective stiffness, respectively (For interpretation of the references to colour in this figure legend, readers are referred to the web version of this article).

To construct the frequency band structure of the meta-truss bar, the theoretical dispersion curves obtained from Eq. (19) for wave propagation are illustrated in Fig. 12. It should be noted that the bandgap corresponds to the frequency range when the imaginary part (the attenuation factor) is not equal to zero. As shown, there are three bandgaps in the frequency band structure of the meta-truss bar, with one additional bandgap in the low-frequency region compared to the model without shear stiffness. Specifically, the three bandgaps are 0 – 5 kHz, 9.3 – 11.5 kHz, and >13.5 kHz. In these frequency ranges, no waves can freely propagate through the meta-truss bar. The dividing points of the first and last branches correspond to the locations where the effective mass or effective stiffness becomes zero, respectively. Whereas the dividing points for the middle-frequency band are the combination of both the negative effective mass and negative effective stiffness. It is worth mentioning that the dividing points mean the starting or cutoff frequencies of the bandgaps.

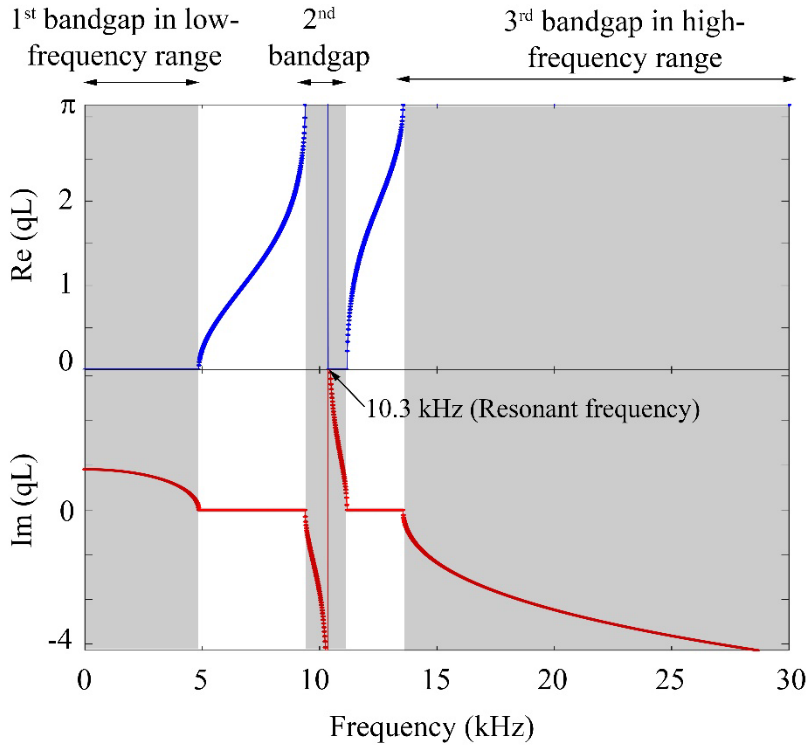

Fig. 12. Complex frequency band structure of the dispersion curves of the spring-mass model with shear stiffness to show the theoretical bandgap regions of metaconcrete including the real part on the upper side and the imaginary part on the lower side. Shaded areas in grey indicate the bandgaps (For interpretation of the references to colour in this figure legend, readers are referred to the web version of this article).

To further validate the above theoretical predictions, a numerical model of the considered meta-truss bar is developed in the commercial FEA software, LS-Dyna. The design of the considered meta-truss bar consists of 8 unit cells, whose dimensions and compositions are depicted in Fig.

10. The transmission coefficient is numerically calculated and compared with the theoretical predictions. The transmission coefficient is the ratio between the output and the input signals of the considered meta-truss bar. For the numerical simulation, the input signal defined by a sweep frequency ranging from 0 – 30 kHz is applied at one end of the meta-lattice truss, and the output response at the other end is captured to calculate the transmission coefficient. All elements in the numerical model, i.e. solid hexahedron elements (SOLID 164), are meshed with a minimum meshing size of 1 mm after performing mesh convergence tests. Details of the mesh size sensitivity analysis with the same structure have been reported in the previous study [25], which is therefore not repeated here for brevity. For modelling contact and boundary conditions, the interfaces between the inclusions and coating defined by the keyword *TIED_SURFACE_TO_SURFACE are assumed as perfect contact while the keyword *NON_REFLECTING_BOUNDARY is applied at one end of the model to minimize stress waves reflection. The material properties used in the numerical model are the same as those in theoretical calculations given in Table 2.

The transmission coefficient profiles from the analytical analysis and numerical simulation are shown in Fig. 13. The bandgaps from the analytical transmission coefficient are the same as those obtained from the dispersive analysis and the effective mass and stiffness. As shown, the bandgap regions corresponding to the wave reduction in the transmission-frequency profiles from the analytical prediction match very well with those from numerical simulation, further confirming the validity of the analytical model for predicting the bandgaps of the meta-truss bar. It should be noted that the locally resonant frequency of the resonator (i.e. 10.3 kHz) corresponds to a big dip displacement in the transmission profile. From the numerical simulation, the first and second bandgaps are respectively at 0 kHz to 4.1 kHz and 8.5 kHz to 12.3 kHz while the high-frequency bandgap is greater than 14.2 kHz. It is found that the first bandgaps between the two approaches agree reasonably well. The discrepancies between the numerical and the analytical results can be attributed to the assumption of the infinite number of unit cores in the theoretical derivations while only 8 unit cores are modelled in the numerical simulation, and likely numerical errors because of discretization. It should be worth mentioning that there are slight variations between the model with 8 unit cells and other numbers of unit cells in terms of the location of the bandgap and the bandwidth. Although the numerical model with more unit cells yields a bit more accurate prediction with the analytical results compared with that with 8 unit cells, considering both the accuracy and computational cost, the numerical model with 8 unit cells is chosen in this study.

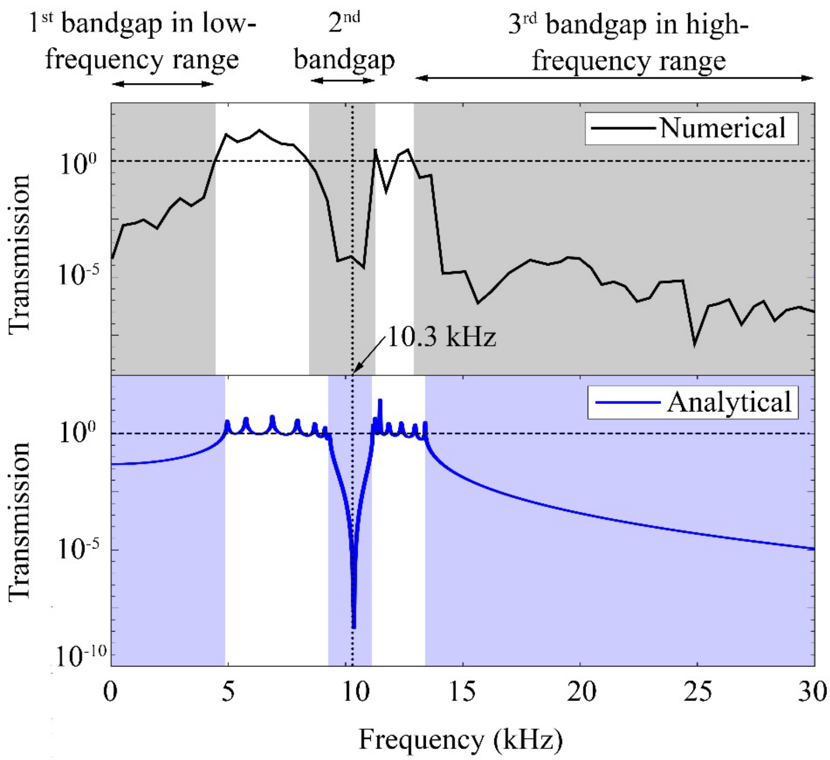

Fig. 13. Transmission coefficient against frequency of excitation for validation between numerical and analytical results. Shaded areas in blue and grey indicate the bandgaps associated with the analytical analysis and numerical analysis, respectively (For interpretation of the references to colour in this figure legend, readers are referred to the web version of this article).

The above analyses have proven the considered meta-truss bar can generate three bandgaps and it can mitigate stress wave propagation when the wave frequency falls within these bandgaps. To demonstrate the frequency-filtering performance of the meta-truss bar in the low-frequency range, a harmonic displacement input constituted by three frequencies, i.e. $u(t)=\sum_{i=1}^{3}\sin\left(2\pi f_i t\right)$, where f_1=1 kHz, f_2= 3 kHz, and f_3= 7 kHz, is applied to the input end of the meta-truss bar to examine whether the wave could propagate through the meta-truss bar. The displacement at the other end is recorded as the output signal. It should be noted that f_1 and f_2 are deliberately selected to fall within the first bandgap in the low-frequency range of the meta-truss bar, while f_3 does not fall into any bandgap. Fig. 14 shows the Fast Fourier Transform (FFT) spectra of displacement-time histories at the two ends of the meta-truss bar (i.e. the input and the output, respectively). As shown, a significant wave reduction in the first bandgap is observed as expected with only the input signal at 7 kHz passing through the meta-truss bar while the other two components at 1 kHz and 3 kHz within the first bandgap are effectively mitigated. Generally, the obtained results indicate that the meta-truss bar has the favourable ability to filter stress waves with frequency contents falling in its bandgap.

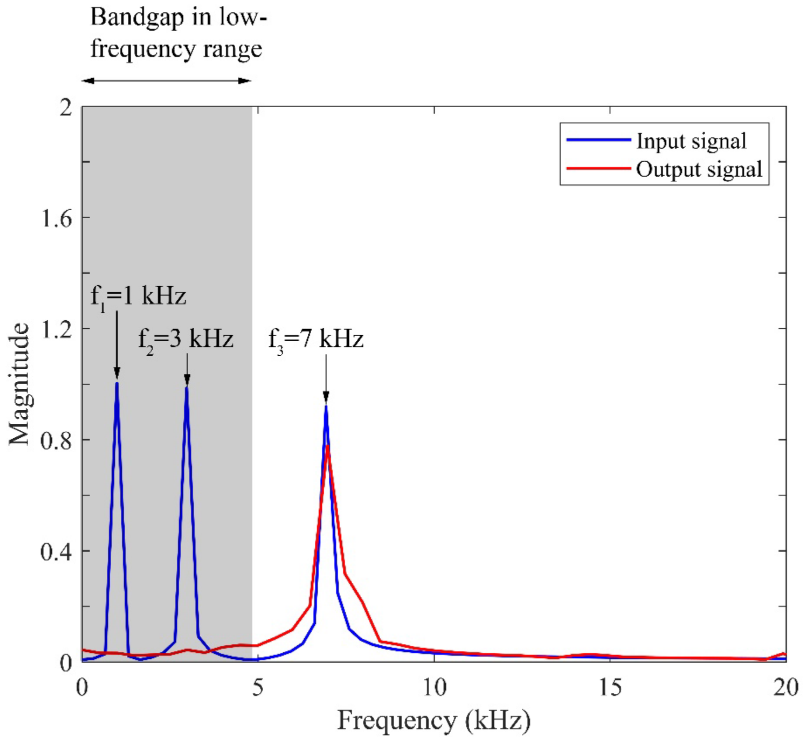

Fig. 14. FFT spectra of the input and output displacements at center points of two ends of the meta-truss bar. Input prescribed displacement is applied to one end of the meta-truss bar while the output displacement is captured at the other end. The displacements of the input and output respectively denoted by the blue solid line and red dotted line are illustrated in (a) time histories and (b) FFT spectra. (For interpretation of the references to colour in this figure legend, readers are referred to the web version of this article).

3.3 Discussions

Recall the two issues that are defined and discussed in the above sections, namely one or two bandgaps obtained in the metaconcrete in previous analyses by different researchers, and the existence of an additional low-frequency bandgap in the meta-truss bar. Based on the above results, these two issues are discussed here.

For the first issue, it is clear now that the analysis that considers only the negative effective mass in determining the bandgap of the metaconcrete fails to obtain the second high-frequency bandgap associated with the negative effective stiffness. Neglecting the influence of the negative effective stiffness also results in an under-prediction of the width of the first bandgap. Therefore both the negative effective mass and negative effective stiffness need to be considered in determining the bandgaps of metaconcrete. The predicted bandgaps with consideration of both the negative effective mass and stiffness agree well with those obtained in experimental tests, verifying the correctness of the proposed analytical model.

For the second issue, it is clear that if the shear resistance exists between the unit cells and the matrix, a low-frequency bandgap will be generated. In such cases, the metastructure could have three bandgaps for wave propagation mitigation. The formation of the low-frequency bandgap is of significant importance for practical applications since many loadings on civil, mechanical, and other structures have low-frequency contents. To facilitate engineering applications, a design procedure for meta-panel is presented in the appendix.

In brief, the actual realizations of the predicted bandgaps of resonance-based metamaterials/metastructures are presented in this study. The results demonstrate that the analytical model can accurately predict the experimental bandgaps of the metaconcrete, including one widened middle bandgap compared to the conventional analysis and another bandgap in the high-frequency range. It is found that at the resonance frequency, a merging bandgap from both the negative effective mass and negative effective stiffness is formed, corresponding to the out-of-phase motions of the resonators. In addition, the meta-truss bar is proven to possess the bandgap in the low-frequency range due to the shear stiffness between the soft coating layers and the truss tube. With such unique capabilities, physically realizable waveguide at different frequencies can be programmably designed for metamaterials/metastructures for numerous practical engineering applications.

4. Conclusions

This study presents an in-depth analysis of the bandgap formation in metaconcrete and meta-truss bar. The effective mass and effective stiffness, the wave dispersion relation, and the transmission coefficient are analytically derived to quantitatively determine the bandgaps of the metaconcrete and meta-truss bar. The analytical outputs are validated against experimental results and numerical predictions. Two bandgaps exist in metaconcrete structure, in which the first bandgap is formed by the negative effective mass and the negative effective stiffness while the negative effective stiffness further creates another bandgap in the high-frequency range. The shear stiffness between the cores and the surrounding host matrix governs an additional bandgap in the low-frequency range in the meta-truss bar. This bandgap only appears when the shear behaviour between the cores and the host matrix is considerable. In addition, this study also provides a detailed design as an example in the appendix for programmable waveguides of the meta-panel consisting of meta-truss bars, which can be employed for designing the meta-panel for mitigation of dynamic loading effect.

Acknowledgments

The authors would like to acknowledge the financial support from Australian Research Council via Laureate Fellowships FL180100196. The first author also acknowledges the support through Research Training Program Scholarship (RTP) from Australian Government.

References

[1] V. Richman, M.R. Santos, J.T. Barkoulas, SHORT- AND LONG-TERM EFFECTS OF THE 9/11 EVENT: THE INTERNATIONAL EVIDENCE, International Journal of Theoretical and Applied Finance, 08 (2005) 947-958.
[2] S. Al-Hajj, H.R. Dhaini, S. Mondello, H. Kaafarani, F. Kobeissy, R.G. DePalma, Beirut Ammonium Nitrate Blast: Analysis, Review, and Recommendations, 9 (2021).
[3] N.S. Ha, G. Lu, A review of recent research on bio-inspired structures and materials for energy absorption applications, Compos Part B: Eng, 181 (2020) 107496.

[4] N.S. Ha, G. Lu, D. Shu, T.X. Yu, Mechanical properties and energy absorption characteristics of tropical fruit durian (Durio zibethinus), Journal of the Mechanical Behavior of Biomedical Materials, 104 (2020) 103603.
[5] N.S. Ha, G. Lu, X. Xiang, High energy absorption efficiency of thin-walled conical corrugation tubes mimicking coconut tree configuration, Int J Mech Sci, 148 (2018) 409-421.
[6] N.S. Ha, G. Lu, X. Xiang, Energy absorption of a bio-inspired honeycomb sandwich panel, J. Mater. Sci., 54 (2019) 6286-6300.
[7] N.S. Ha, G. Lu, Thin-walled corrugated structures: A review of crashworthiness designs and energy absorption characteristics, Thin-Walled Structures, 157 (2020) 106995.
[8] N.S. Ha, T.M. Pham, W. Chen, H. Hao, G. Lu, Crashworthiness analysis of bio-inspired fractal tree-like multi-cell circular tubes under axial crushing, Thin-Walled Structures, 169 (2021) 108315.
[9] N.S. Ha, T.M. Pham, H. Hao, G. Lu, Energy absorption characteristics of bio-inspired hierarchical multi-cell square tubes under axial crushing, Int J Mech Sci, 201 (2021) 106464.
[10] V.G. Veselago, The Electromanatics of Substances with Simultaneously Negative Value of e and μ, Soviet Physics Uspekhi, 10 (1968) 509-514.
[11] Y. Chen, G. Hu, G. Huang, A hybrid elastic metamaterial with negative mass density and tunable bending stiffness, J. Mech. Phys. Solids., 105 (2017) 179-198.
[12] Z. Li, Q. Yang, R. Fang, W. Chen, H. Hao, Origami metamaterial with two-stage programmable compressive strength under quasi-static loading, Int J Mech Sci, 189 (2021) 105987.
[13] C. Comi, L. Driemeier, Wave propagation in cellular locally resonant metamaterials, Lat. Am. J. Solid. Struct., 15 (2018).
[14] X. Zhou, X. Liu, G. Hu, Elastic metamaterials with local resonances: an overview, Theoretical and Applied Mechanics Letters, 2 (2012) 041001.
[15] S. Lin, Y. Zhang, Y. Liang, Y. Liu, C. Liu, Z. Yang, Bandgap characteristics and wave attenuation of metamaterials based on negative-stiffness dynamic vibration absorbers, J. Sound. Vib., 502 (2021) 116088.
[16] X. Xiang, Z. Fu, S. Zhang, G. Lu, N.S. Ha, Y. Liang, X. Zhang, The mechanical characteristics of graded Miura-ori metamaterials, Mater. Des., 211 (2021) 110173.
[17] A. Banerjee, R. Das, E.P. Calius, Frequency graded 1D metamaterials: A study on the attenuation bands, J. Appl. Phys., 122 (2017) 075101.
[18] X. Xu, M.V. Barnhart, X. Li, Y. Chen, G. Huang, Tailoring vibration suppression bands with hierarchical metamaterials containing local resonators, J. Sound. Vib., 442 (2019) 237-248.
[19] C. Cai, Z. Wang, Y. Chu, G. Liu, Z. Xu, The phononic band gaps of Bragg scattering and locally resonant pentamode metamaterials, J. Phys. D: Appl. Phys., 50 (2017) 415105.
[20] T. Lee, H. Iizuka, Bragg scattering based acoustic topological transition controlled by local resonance, Physical Review B, 99 (2019) 064305.
[21] Y. Xiao, J. Wen, G. Wang, X. Wen, Theoretical and Experimental Study of Locally Resonant and Bragg Band Gaps in Flexural Beams Carrying Periodic Arrays of Beam-Like Resonators, 2013.
[22] A.O. Krushynska, M. Miniaci, F. Bosia, N.M. Pugno, Coupling local resonance with Bragg band gaps in single-phase mechanical metamaterials, Extreme Mechanics Letters, 12 (2017) 30-36.
[23] M. Cenedese, E. Belloni, F. Braghin, Interaction of Bragg scattering bandgaps and local resonators in mono-coupled periodic structures, J. Appl. Phys., 129 (2021) 124501.
[24] N.H. Vo, T.M. Pham, K. Bi, H. Hao, Model for analytical investigation on meta-lattice truss for low-frequency spatial wave manipulation, Wave Motion, 103 (2021) 102735.

[25] N.H. Vo, T.M. Pham, K. Bi, W. Chen, H. Hao, Stress Wave Mitigation Properties of Dual-meta Panels against Blast Loads, Int J Impact Eng, 154 (2021) 103877.
[26] N.H. Vo, T.M. Pham, H. Hao, K. Bi, W. Chen, N.S. Ha, Blast resistant enhancement of meta-panels using multiple types of resonators, Int J Mech Sci, 215 (2022) 106965.
[27] G. Hu, L. Tang, R. Das, S. Gao, H. Liu, Acoustic metamaterials with coupled local resonators for broadband vibration suppression, AIP Adv., 7 (2017) 025211.
[28] L.-Z. Huang, Y. Xiao, J.-H. Wen, H.-B. Yang, X.-S. Wen, Analysis of underwater decoupling properties of a locally resonant acoustic metamaterial coating, Chinese Physics B, 25 (2016) 024302.
[29] H. Meng, N. Bailey, Y. Chen, L. Wang, F. Ciampa, A. Fabro, D. Chronopoulos, W. Elmadih, 3D rainbow phononic crystals for extended vibration attenuation bands, Sci. Rep., 10 (2020) 18989.
[30] J.H. Oh, S.J. Choi, J.K. Lee, Y.Y. Kim, Zero-frequency Bragg gap by spin-harnessed metamaterial, New J. Phys., 20 (2018) 083035.
[31] Y.Y. Zhang, N.S. Gao, G.S. Xu, J.H. Wu, M. Cao, Z.T. Zhou, Low-frequency band gaps within a local resonance structures, Mod. Phys. Lett. B, 34 (2020) 2150014.
[32] T.N.T. Cao, V.H. Luong, H.N. Vo, X.V. Nguyen, V.N. Bui, M.T. Tran, K.K. Ang, A Moving Element Method for the Dynamic Analysis of Composite Plate Resting on a Pasternak Foundation Subjected to a Moving Load, International Journal of Computational Methods, 16 (2018) 1850124.
[33] P. Sheng, X.X. Zhang, Z. Liu, C.T. Chan, Locally resonant sonic materials, Physica B: Condensed Matter, 338 (2003) 201-205.
[34] P. Wang, F. Casadei, S. Shan, J.C. Weaver, K. Bertoldi, Harnessing Buckling to Design Tunable Locally Resonant Acoustic Metamaterials, Phys. Rev. Lett., 113 (2014) 014301.
[35] A. Palermo, M. Vitali, A. Marzani, Metabarriers with multi-mass locally resonating units for broad band Rayleigh waves attenuation, Soil Dynamics and Earthquake Engineering, 113 (2018) 265-277.
[36] G. Hu, L. Tang, J. Xu, C. Lan, R. Das, Metamaterial With Local Resonators Coupled by Negative Stiffness Springs for Enhanced Vibration Suppression, Journal of Applied Mechanics, 86 (2019).
[37] M. Yang, P. Sheng, Sound Absorption Structures: From Porous Media to Acoustic Metamaterials, 2017.
[38] G. Finocchio, O. Casablanca, G. Ricciardi, U. Alibrandi, F. Garescì, M. Chiappini, B. Azzerboni, Seismic metamaterials based on isochronous mechanical oscillators, Appl. Phys. Lett., 104 (2014) 191903.
[39] Y.Y. Chen, M.V. Barnhart, J.K. Chen, G.K. Hu, C.T. Sun, G.L. Huang, Dissipative elastic metamaterials for broadband wave mitigation at subwavelength scale, Compos. Struct., 136 (2016) 358-371.
[40] N.H. Vo, T. Pham, K. Bi, W. Chen, H. Hao, Impact Load Mitigation of Meta-panels with Single Local Resonator, Eng. Struct., Under Review (2021).
[41] K.K. Reichl, D.J. Inman, Lumped mass model of a 1D metastructure for vibration suppression with no additional mass, J. Sound. Vib., 403 (2017) 75-89.
[42] Y. Liu, X. An, H. Chen, H. Fan, Vibration attenuation of finite-size metaconcrete: Mechanism, prediction and verification, Composites Part A: Applied Science and Manufacturing, 143 (2021) 106294.
[43] J. Huang, Z. Shi, Attenuation zones of periodic pile barriers and its application in vibration reduction for plane waves, J. Sound. Vib., 332 (2013) 4423-4439.
[44] R. Zhu, X.N. Liu, G.K. Hu, C.T. Sun, G.L. Huang, A chiral elastic metamaterial beam for broadband vibration suppression, J. Sound. Vib., 333 (2014) 2759-2773.

[45] G. Hu, L. Tang, A. Banerjee, R. Das, Metastructure With Piezoelectric Element for Simultaneous Vibration Suppression and Energy Harvesting, J. Vib. Acoust., 139 (2016) 011012-011012-011011.
[46] Y. Yan, A. Laskar, Z. Cheng, F. Menq, Y. Tang, Y.L. Mo, Z. Shi, Seismic isolation of two dimensional periodic foundations, J. Appl. Phys., 116 (2014) 044908.
[47] Y. Yan, Z. Cheng, F. Menq, Y.L. Mo, Y. Tang, Z. Shi, Three dimensional periodic foundations for base seismic isolation, Smart Mater. Struct., 24 (2015) 075006.
[48] M. Miniaci, A. Krushynska, F. Bosia, N.M. Pugno, Large scale mechanical metamaterials as seismic shields, New J. Phys., 18 (2016) 083041.
[49] Z. Shi, Z. Cheng, H. Xiang, Seismic isolation foundations with effective attenuation zones, Soil Dynamics and Earthquake Engineering, 57 (2014) 143-151.
[50] A.O. Krushynska, A. Amendola, F. Bosia, C. Daraio, N.M. Pugno, F. Fraternali, Accordion-like metamaterials with tunable ultra-wide low-frequency band gaps, New J. Phys., 20 (2018) 073051.
[51] Q. Zhang, K. Zhang, G. Hu, Tunable fluid-solid metamaterials for manipulation of elastic wave propagation in broad frequency range, Appl. Phys. Lett., 112 (2018) 221906.
[52] Y. Liu, X. Shen, X. Su, C.T. Sun, Elastic Metamaterials With Low-Frequency Passbands Based on Lattice System With On-Site Potential, J. Vib. Acoust., 138 (2016) 021011-021011-021010.
[53] S. Yao, X. Zhou, G. Hu, Experimental study on negative effective mass in a 1D mass–spring system, New J. Phys., 10 (2008) 043020.
[54] S.J. Mitchell, A. Pandolfi, M. Ortiz, Metaconcrete: designed aggregates to enhance dynamic performance, J. Mech. Phys. Solids., 65 (2014) 69-81.
[55] C. Xu, W. Chen, H. Hao, The influence of design parameters of engineered aggregate in metaconcrete on bandgap region, J. Mech. Phys. Solids., 139 (2020) 103929.
[56] C. Xu, W. Chen, H. Hao, K. Bi, T.M. Pham, Experimental and numerical assessment of stress wave attenuation of metaconcrete rods subjected to impulsive loads, Int J Impact Eng, 159 (2022) 104052.
[57] C. Xu, W. Chen, H. Hao, H. Jin, Effect of engineered aggregate configuration and design on stress wave attenuation of metaconcrete rod structure, International Journal of Solids and Structures, 232 (2021) 111182.
[58] C. Ding, L. Hao, X. Zhao, Two-dimensional acoustic metamaterial with negative modulus, J. Appl. Phys., 108 (2010) 074911.
[59] X. Zhou, G. Hu, Analytic model of elastic metamaterials with local resonances, Physical Review B, 79 (2009) 195109.
[60] S.H. Lee, C.M. Park, Y.M. Seo, Z.G. Wang, C.K. Kim, Acoustic metamaterial with negative modulus, J. Phys.: Condens. Matter, 21 (2009) 175704.
[61] S.H. Lee, C.M. Park, Y.M. Seo, Z.G. Wang, C.K. Kim, Composite Acoustic Medium with Simultaneously Negative Density and Modulus, Phys. Rev. Lett., 104 (2010) 054301.
[62] X.N. Liu, G.K. Hu, G.L. Huang, C.T. Sun, An elastic metamaterial with simultaneously negative mass density and bulk modulus, Appl. Phys. Lett., 98 (2011) 251907.
[63] Y.-F. Wang, Y.-S. Wang, V. Laude, Wave propagation in two-dimensional viscoelastic metamaterials, Physical Review B, 92 (2015) 104110.
[64] A.O. Krushynska, V.G. Kouznetsova, M.G.D. Geers, Towards optimal design of locally resonant acoustic metamaterials, J. Mech. Phys. Solids., 71 (2014) 179-196.
[65] D. Lee, D.M. Nguyen, J. Rho, Acoustic wave science realized by metamaterials, Nano Convergence, 4 (2017) 3.
[66] C. Xu, W. Chen, H. Hao, T.M. Pham, K. Bi, Damping properties and dynamic responses of metaconcrete beam structures subjected to transverse loading, Constr. Build. Mater., 311 (2021) 125273.

[67] H. Jin, H. Hao, Y. Hao, W. Chen, Predicting the response of locally resonant concrete structure under blast load, Constr. Build. Mater., 252 (2020) 118920.
[68] M.M. Hajjaj, J. Tu, A seismic metamaterial concept with very short resonators using depleted uranium, Archive of Applied Mechanics, (2021).
[69] S. Fujikura, M. Bruneau, Experimental Investigation of Seismically Resistant Bridge Piers under Blast Loading, J. Bridge Eng., 16 (2011) 63-71.
[70] S. Krödel, N. Thomé, C. Daraio, Wide band-gap seismic metastructures, Extreme Mechanics Letters, 4 (2015) 111-117.
[71] C. Kettenbeil, G. Ravichandran, Experimental investigation of the dynamic behavior of metaconcrete, Int J Impact Eng, 111 (2018) 199-207.
[72] S.J. Mitchell, A. Pandolfi, M. Ortiz, Investigation of elastic wave transmission in a metaconcrete slab, Mech. Mater., 91 (2015) 295-303.

Appendix

A. Design guide for meta-truss bars with targeted bandgap regions

Based on the above analytical solutions, a design method of meta-truss bars with the desired target bandgaps is proposed in this section. The proposed design flowchart is illustrated in Fig. 15. It starts with the parameters of the expected loading F(t) on the considered structure. This loading can be a recorded impact load, blast load or load given in a design code. The next step is to determine the frequency content of F(t) using the Fast Fourier Transform (FFT). From the FFT spectrum of the design load, the desired bandgaps, $BG_i=[f_{i1}-f_{i2}]$, can be determined to ideally cover the entire or primary frequency ranges that the loading energy distributed in the frequency domain for the best loading mitigation effect. It should be noted that the subscript i=1,2,3 indicates the first, second, and third bandgaps of the meta-truss bar and ideally BG_i should enclose all frequency ranges $[f_a,\ldots,f_b]$ that loading energy distributes to achieve the maximal mitigation effect. The design parameters of the spring-mass model, i.e. m_i and k_i, are analytically calculated based on the theoretical bandgap starting point f_{i1} and cutoff point f_{i2}, which will be discussed later in Appendix B. Next, the initial design features including geometric parameters, materials are selected as given in Eq. (23). After the initial selection of the design parameters, the bandgaps of the meta-truss bar are numerically evaluated using a numerical verification, e.g. using LS-Dyna. If the calculated bandgaps from the initial selection meet the above requirements, it shall move to the final step. If not, the trial and error processes are required to obtain the appropriate design parameters ensuring that the numerical bandgaps cover all or primary frequency contents of the applied loading. Finally, given a set of design parameters, the meta-structures can be fabricated.

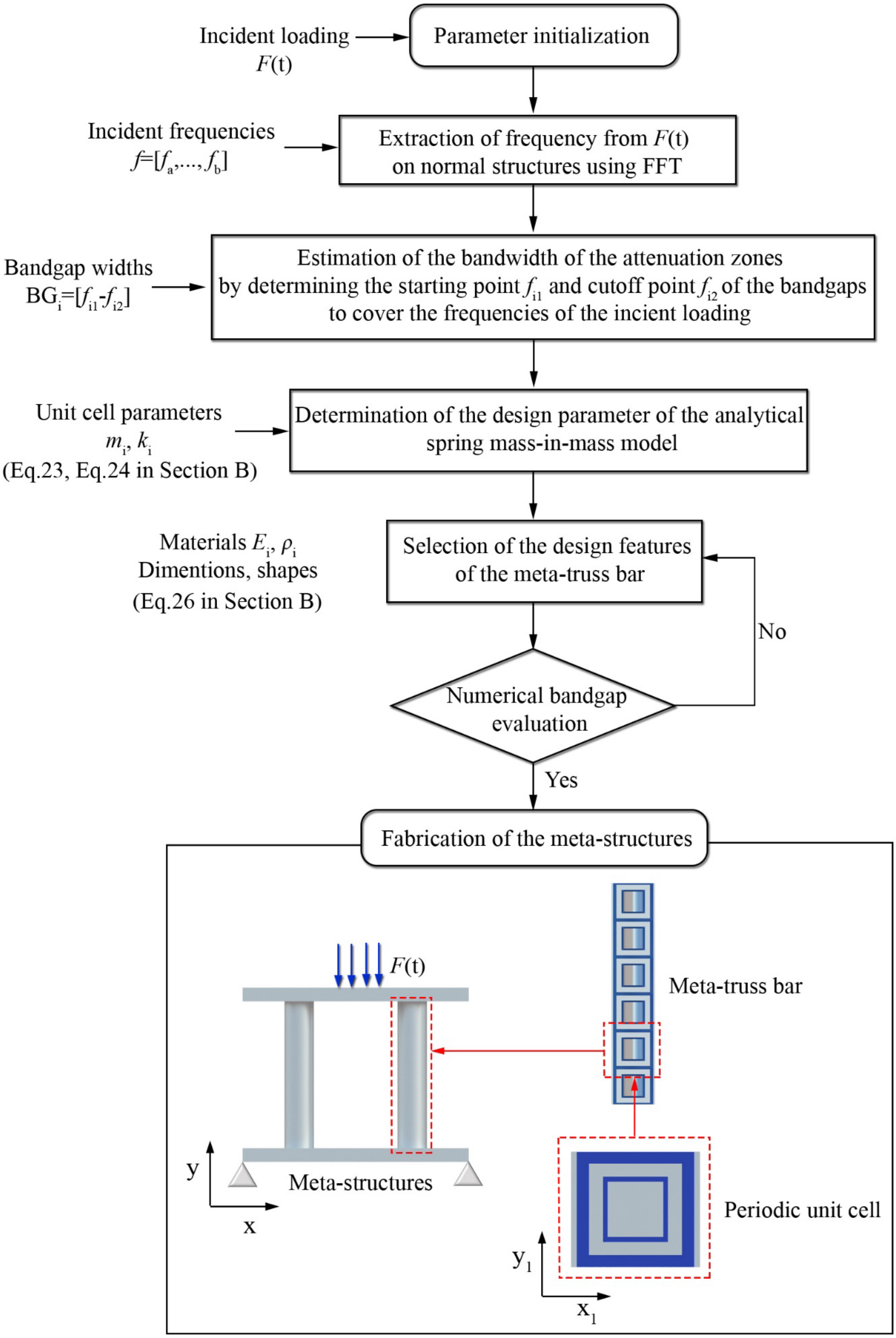

Incident loading
F(t)
Parameter initialization
Incident frequencies
f=[f_a,...,f_b]
Extraction of frequency from F(t) on normal structures using FFT
Bandgap widths
BG_i=[f_i1-f_i2]
Estimation of the bandwidth of the attenuation zones by determining the starting point f_i1 and cutoff point f_i2 of the bandgaps to cover the frequencies of the incient loading
Unit cell parameters
m_i, k_i
(Eq.23, Eq.24 in Section B)
Determination of the design parameter of the analytical spring mass-in-mass model
Materials E_i, ρ_i
Dimentions, shapes
(Eq.26 in Section B)
Selection of the design features of the meta-truss bar
No
Numerical bandgap evaluation
Yes
Fabrication of the meta-structures
F(t)
Meta-truss bar
y
x
Meta-structures
Periodic unit cell
y1
x1

Fig. 15. Flowchart of the meta-structure design consists 7 steps starting with the parameter initialization and ending with the meta-panel fabrication.

B. Determination of the Starting and Cutoff frequencies of a corresponding bandgap

The bandgaps from the comprehensive analysis of the spring-mass model are presented in Fig. 16. Based on the theoretical results from this study, the bandgaps of the meta-truss bar can be divided into three regions including [0-f_{11}] for the 1st bandgap, [f_{21}-f_{22}] for the 2nd bandgap, and [>f_{31}] for the 3rd bandgap. It is worth mentioning that the local resonant frequency of the resonator can be calculated by, $f_0 = \sqrt{\frac{k_{a2}+k_{s2}}{m_2}}/(2\pi)$.

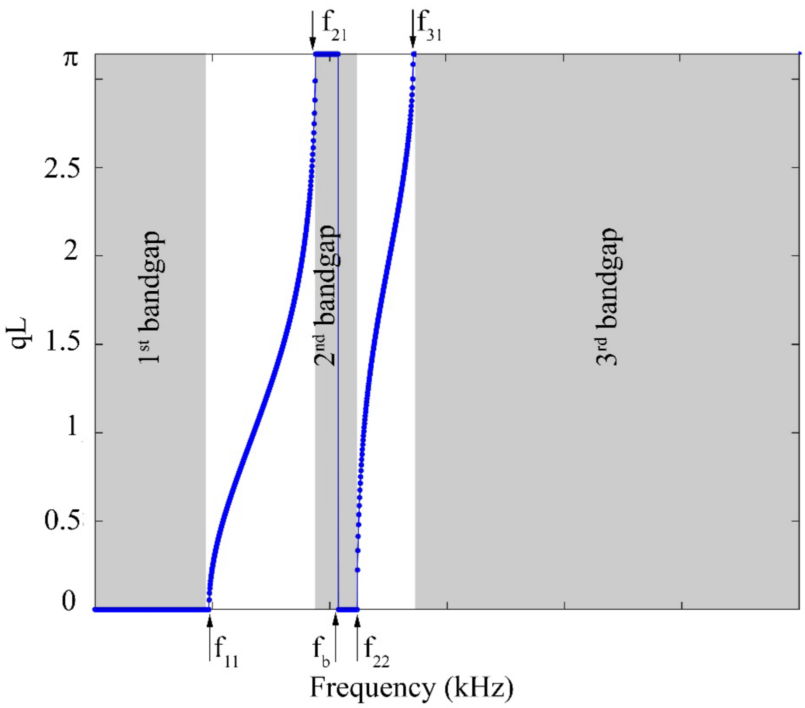

Fig. 16. Typical bandgap determination based on the dispersion curves is divided into three regions including [0-f_{11}] for the 1st bandgap, [f_{21}-f_{22}] for the 2nd bandgap, and [>f_{31}] for the 3rd bandgap. (For interpretation of the references to colour in this figure legend, readers are referred to the web version of this article).

To define the width of the bandgaps, the dispersion in Eq. (19) can be rewritten as

$$m_1 m_2 \omega^4 - \left[2m_2\left(1-\cos qL\right)k_{a1} + m_2 k_{s1} + \left(m_1+m_2\right)k_{a2} + m_1 k_{s2}\right]\omega^2 + \\ +2k_{a1}\left(k_{a2}+k_{s2}\right)\left(1-\cos qL\right) + k_{s1}\left(k_{a1}+k_{s2}\right) + k_{a2}k_{s2} = 0 \tag{21}$$

The expression of the angular frequency can be obtained by solving Eq. (21) as

$$\omega^2 = \frac{2m_2\left(1-\cos qL\right)k_{a1} + m_2 k_{s1} + \left(m_1+m_2\right)k_{a2} + m_1 k_{s2} \pm \sqrt{\Psi - \mathrm{X}}}{2m_1 m_2} \tag{22}$$

where $\Psi = \left(2m_2\left(1-\cos qL\right)k_{a1} + m_2 k_{s1} + \left(m_1+m_2\right)k_{a2} + m_1 k_{s2}\right)^2$ and $\mathrm{X} = 4m_1 m_2\left[2k_{a1}\left(k_{a2}+k_{s2}\right)\left(1-\cos qL\right) + k_{s1}\left(k_{a2}+k_{s2}\right) + k_{a2}k_{s2}\right]$

The starting angular frequencies of the bandgaps can be obtained by substituting qL=0, as

$$\omega_{i1}^2 = \frac{m_2 k_{s1} + \left(m_1+m_2\right)k_{a2} + m_1 k_{s2} \pm \sqrt{\Gamma}}{2m_1 m_2}, \ i=1,2,3 \tag{23}$$

where $\Gamma = \left(m_2 k_{s1} + \left(m_1+m_2\right)k_{a2} + m_1 k_{s2}\right)^2 - 4m_1 m_2\left[k_{s1}\left(k_{a2}+k_{s2}\right) + k_{a2}k_{s2}\right]$

The cutoff angular frequencies of the bandgaps can be obtained by substituting qL=π, as

$$\omega_{i2}^2 = \frac{4m_2 k_{a1} + m_2 k_{s1} + \left(m_1+m_2\right)k_{a2} + m_1 k_{s2} \pm \sqrt{\Lambda - \mathrm{M}}}{2m_1 m_2}, \ i=1,2,3 \tag{24}$$

where $\Lambda = \left(4m_2 k_{a1} + m_2 k_{s1} + \left(m_1+m_2\right)k_{a2} + m_1 k_{s2}\right)^2$ and $\mathrm{M} = 4m_1 m_2\left[4k_{a1}\left(k_{a2}+k_{s2}\right) + k_{s1}\left(k_{a2}+k_{s2}\right) + k_{a2}k_{s2}\right]$

The starting and cutoff frequencies of the bandgaps are

$$f_{ij} = \frac{\omega_{ij}}{2\pi}, \ i=1,2,3 \text{ and } j=1,2,3 \tag{25}$$

The design parameters including internal mass, external mass and stiffnesses can be estimated by Eq. (26), where ρ_i and V_i are the material density and volume of the unit cell, and its length and radius are denoted by l_i and r_i, respectively.

$$m_i = \rho_i V_i = \rho_i \pi r_i^2 l_i \text{, } i=1,2 \tag{26}$$

$$k_{ai} = \frac{EA_i}{l_i} \text{, } k_{si} = \frac{GA_i}{l_i}$$

where E and A are Young's modulus and the nominal cross-section area of the coating material.

C. Worked-out example

A design example of a meta-panel consisting of four meta-truss bars to resist the impact force induced by a spherical ball with a mass of 1 kg and an impact velocity of 30 m/s is presented here to illustrate the above-proposed design procedure.

- Step 1: Determination of the design load F(t).

The impactor has a spherical shape of 20 mm radius and its weight is 1 kg. The initial velocity of the impactor against the structural panel is 30 m/s. A numerical model is generated in LS-DYNA to predict the impact load on the structure. The predicted impact force-time history F(t) is illustrated in Fig. 17.

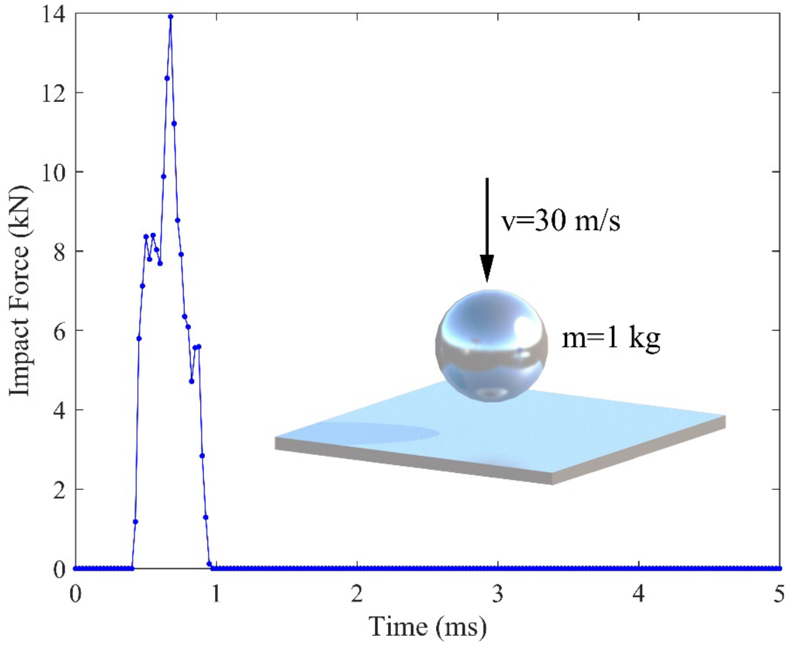

Fig. 17. Peak impact force time history of the simulated impact loading generated by the impactor with the mass of 1kg and the velocity of 30 m/s.

- Step 2: Determination of the frequency contents of *F*(t)

The FFT spectrum of the predicted impact force time history *F*(t) is calculated and shown in Fig. 18. As shown, the impact loading energy distributes mainly in the frequency regions of [0 – 4.8] kHz, [7.5 – 8.5] kHz, and [9.7 – 12] kHz.

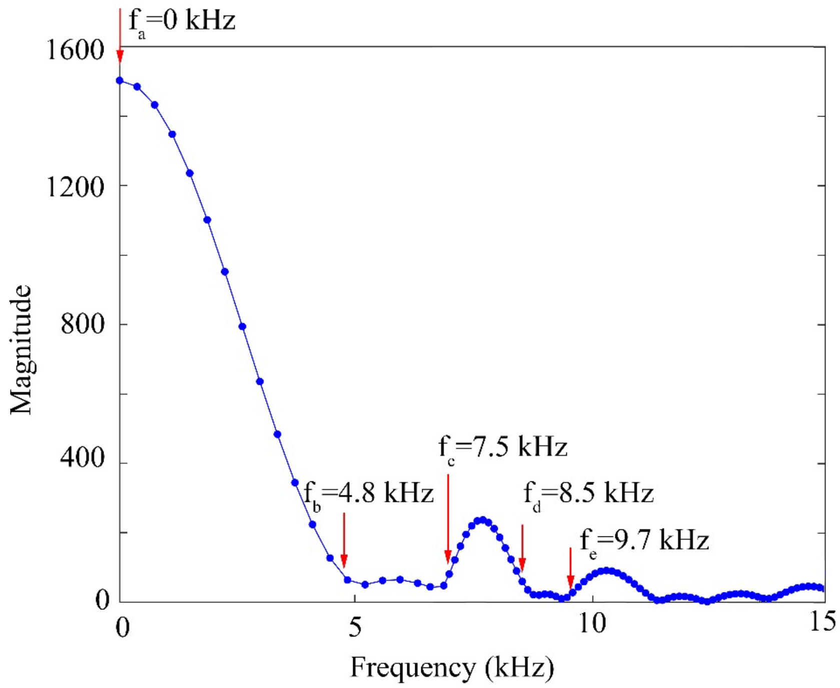

Fig. 18. FFT spectrum of the impact force time history of the simulated impact loading *F*(t) generated by the impactor with the mass of 1kg and the velocity of 30 m/s.

- Step 3: Determinations of the bandwidth of the desired bandgaps to cover the frequencies with the most loading energy.

To cover the dominant frequencies of the applied loading, the bandgaps of the desired meta-truss bar are selected according to the FFT spectrum in Fig. 19 as

$BG_1 = [0 - f_{11}]$ kHz, $BG_2 = [f_{21} - f_{22}]$ kHz, and $BG_3 = [>f_{31}]$ kHz

where f_{11}= 4.8 kHz, f_{21}= 7.5 kHz, f_{22}= 8.5 kHz, and f_{31}= 9.7 kHz.

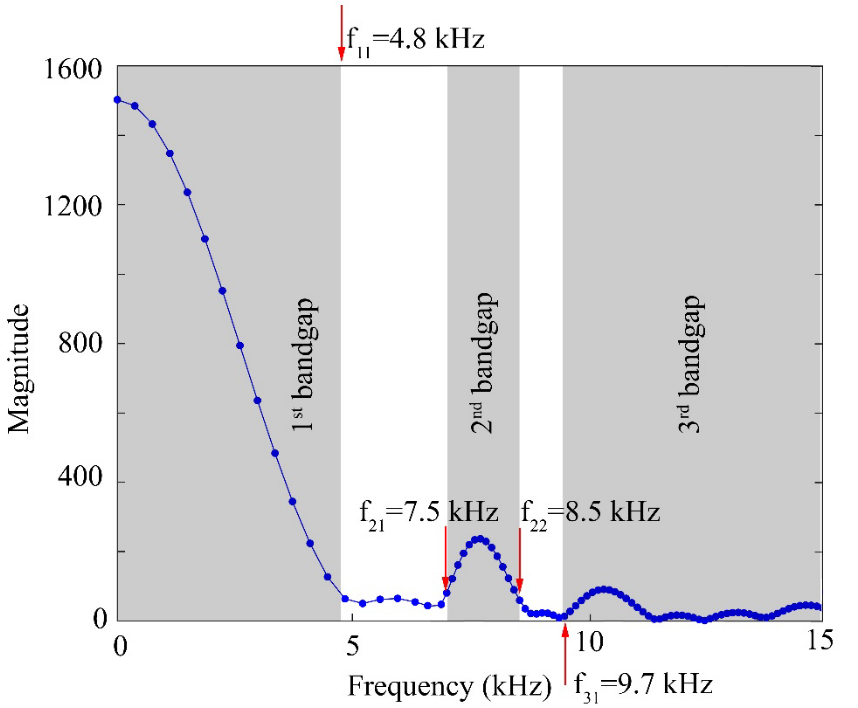

Fig. 19. Estimated bandgap widths of the designed meta-truss bar including [0 – 4.8] kHz for the 1st bandgap, [7.5 – 8.5] kHz for the 2nd bandgap, and [>8.5] kHz for the 3rd bandgap. (For interpretation of the references to colour in this figure legend, readers are referred to the web version of this article).

- Step 4: Calculations of the design parameters

To achieve the above desired bandgaps, the design parameters of the analytical spring-mass model are obtained from Eqs. (23), (24), (25), and they are m_1=4.71x10^{-2} (kg), m_2=1.55x10^{-2} (kg), k_{a1}=2.3x10^8 (N/m), k_{a2}=1.6x10^8 (N/m), k_{s1}=3.2x10^8 (N/m), and k_{s2}=2.3x10^8 (N/m).

- Step 5: Select the materials and dimensions of the meta-truss bar

Polyurethane is selected for the soft coating while the outer tube and the resonators are made of Aluminium and Lead. The diameters of the internal and external resonators are respectively denoted by r_2 and r_1, which are calculated by

$$r_2 = \sqrt{\frac{m_2}{\rho_{Lead}\pi l_2}} = \sqrt{\frac{1.55x10^{-2}}{11400x\pi x12x10^{-9}}} = 6\,(\mathrm{mm})$$

$$r_1 = \sqrt{\left(\frac{m_1}{\rho_{Lead}\pi} + r^2 l\right)\frac{1}{l_1}} = \sqrt{\left(\frac{4.71x10^{-2}}{11400x\pi} + 7^2 x14x10^{-9}\right)\frac{1}{20x10^{-3}}} = 10\,(\text{mm})$$

Thicknesses of the inner and outer coatings, i.e. t_1 and t_2 can be calculated by

$$t_1 = \frac{EA_1}{k_{a1}} = \frac{Ex\pi x r_1^2}{k_{a1}} = \frac{0.147x10^9 x\pi x10^2 x10^{-6}}{2.3x10^8} = 2\,(\text{mm})$$

$$t_2 = \frac{EA_2}{k_{a2}} = \frac{Ex\pi x r_2^2}{k_{a2}} = \frac{0.147x10^9 x\pi x6^2 x10^{-6}}{1.6x10^8} = 1\,(\text{mm})$$

- Step 6: Verification of the bandgaps of the designed meta-truss bar.

To check the bandgaps of the designed meta-truss bar, the above procedures are applied to calculate the bandgap frequencies. Fig. 20 shows the dispersion curves of the meta-truss bar with the above designed dimensions and material properties. As shown, the bandgaps of the designed meta-truss bar cover the primary frequency contents of the applied loading, implying the meta-truss bar is effective to mitigate the loading effects.

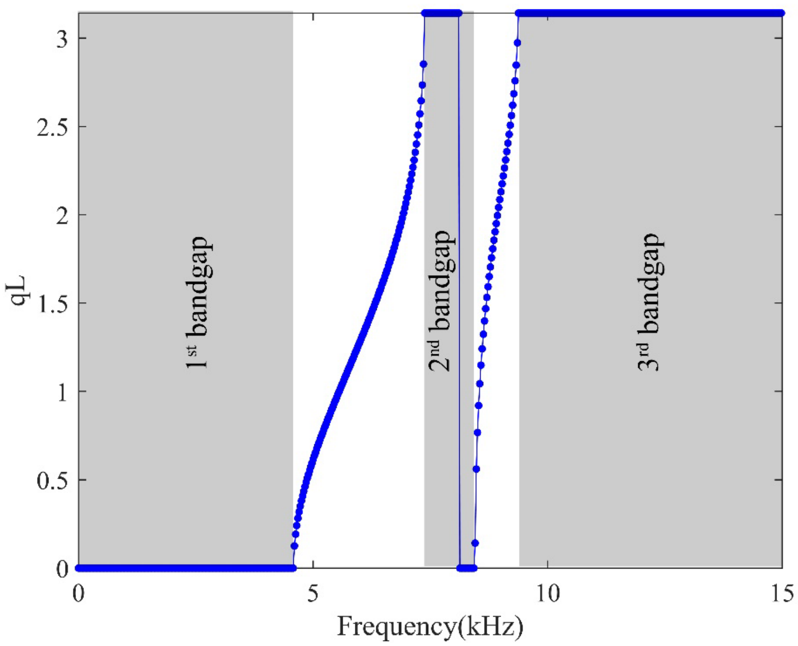

Fig. 20. Dispersion curve of the designed meta-truss bar. Shaded areas in grey indicate the bandgaps (For interpretation of the references to colour in this figure legend, readers are referred to the web version of this article).

- Step 7: Performance of the meta-panel consisting of 4 designed meta-truss bars.

The meta-panel consisting of four designed meta-truss bars is shown in Fig. 21. Its performance in mitigating the impact loading effects is evaluated. The numerical model of the meta-panel is built in LS-DYNA and its impact response is shown in Fig. 22.

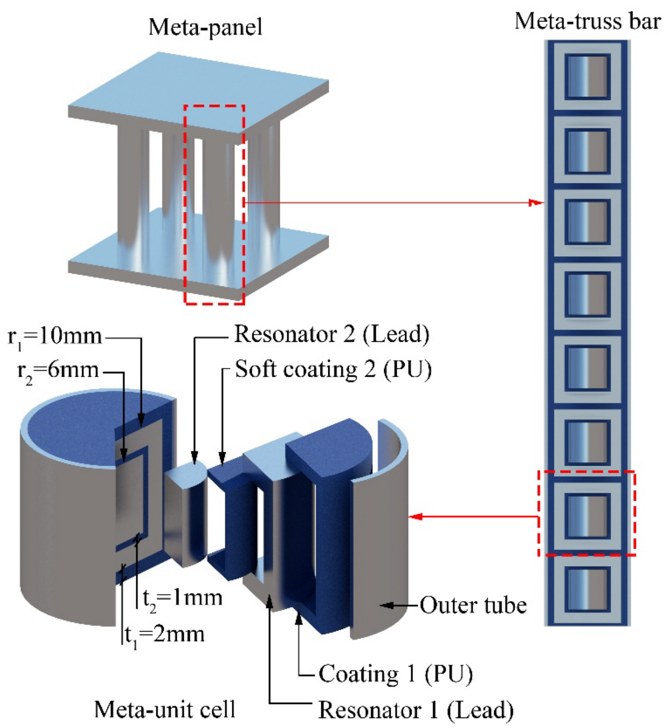

Fig. 21. Design of meta-panel including the schematic view of the meta-panel, meta-unit cell includes the outer tube, the coatings and the resonators, and meta-truss bar is made of 8 unit cells.

As shown, the designed meta-panel functioning as a sacrificial cladding exhibits its superior dynamic performances compared with the traditional designs. In particular, the peak reaction force of the designed meta-panel transmitted to the protected structure is reduced significantly by more than 47% compared to its conventional counterparts including the hollow-truss panel and solid-truss panel. It should be noted that the numerical results from the corresponding panels with solid-truss and hollow-truss bars from [25] was adopted herein for comparison, which is not presented in detail for brevity. More information about these panels can be found in [25]. These results demonstrate that the designed meta-panel yields better protections to structures as compared to the traditional sacrificial panels with solid and hollow truss bars.

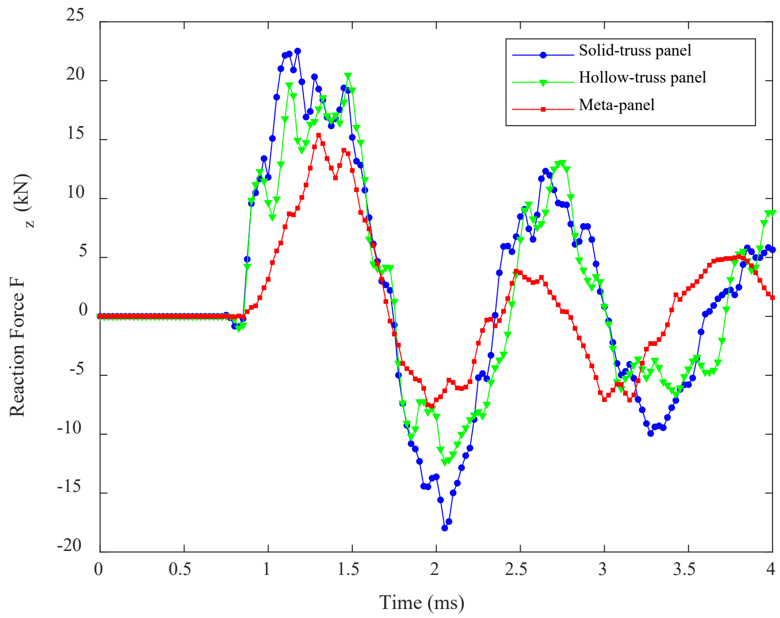

Fig. 22. Comparison of reaction force of the three panels under impact loading. Comparison of reaction force-time history of the back facesheet between the three considered meta-panels including meta-panel, the hollow-truss panel, and the solid-truss panel. (For interpretation of the references to colour in this figure legend, readers are referred to the web version of this article).

D. Determination of axial and shear stiffness of the analytical model

With an attempt to accurately estimate the spring stiffness, the commercial software COMSOL MULTIPHYSICS was adopted. A constant force F which is depicted in Fig. 23 (a) is applied to the model to calculate the value of shear spring stiffness k_{s1} of the internal core while the coupled forces F were put in two directions of the model to estimate the values of k_{a1} as shown in Fig. 23(b). Similarly, the estimation of k_{s2} and k_{a2} is carried out with the same procedure but different dimensions. As seen in Figs. 23 (a-b), the average displacements monitored at the surfaces are denoted as u_i (i=1,2,3,4). It is noted that all edges of the outer shell are clamped. The relation between stiffness and displacement of the unit model is expressed as [25]

$$k_{a1}\left(u_1+u_2\right)+k_{s1}u_1=F \tag{27}$$

$$k_{s1}u_3=F$$

$$k_{a2}\left(u_4+u_5\right)+k_{s2}u_4=F$$

$$k_{s2}u_6=F$$

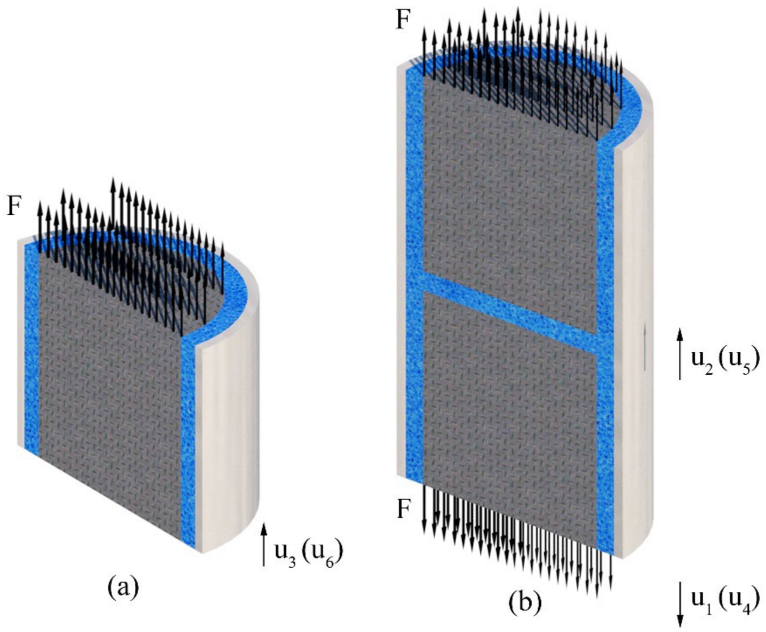

Fig. 23. Outline model utilized for the calculation of (a) k_2 and k_4, and (b) k_1 and k_3.

List of Figures

Fig. 1. Schematic view of metamaterials utilizing (a) Bragg scattering mechanism (e.g. Accordion-like meta-chain of circular discs interlayed by minimal tensegrity prisms, which are formed by tapered bars and prestressed strings [50]) and (b) local resonant mechanism (e.g. tunable fluid-solid metamaterials [51]).

Fig. 2. Schematic view of the discrete spring-mass model adopted for metaconcrete and meta-truss bar in the meta-panel functioning as sacrificial cladding to protect the main structures from blast loading.

Fig. 3. Schematic view of the simplified spring-mass model for metaconcrete, including external mass m_1, internal mass m_2, external axial stiffness k_{a1} and internal axial stiffness k_{a2} with respect to the continuum media and its equivalent effective model with effective mass m_{eff} and effective stiffness k_{eff}.

Fig. 4. Experimental transmission coefficient of the metaconcrete exhibits a high-frequency bandgap not predicted by the conventional approach. Note: the transmission coefficient presented is given by the ratio of the amount of energy transmitted to the last unit to the total energy of the system. (For interpretation of the references to colour in this figure legend, readers are referred to the web version of this article).

Fig. 5. Schematic view of the simplified spring-mass model for meta-truss bar, including external mass m_1, internal mass m_2, external axial stiffness k_{a1}, internal axial stiffness k_{a2}, external shear stiffness k_{s1}, and internal shear stiffness k_{s2} with respect to the continuum media and its equivalent effective model with effective mass m_{eff} and effective stiffness k_{eff}.

Fig. 6. Schematic view of a metaconcrete rod used for modal analysis consisting of 8 unit cells in which each unit cells comprises of the matrix (mortar), the soft coating (nylon) and the spherical inclusion (lead).

Fig. 7. Effective parameters of the spring-mass model to show the theoretical bandgap regions of metaconcrete including the effective mass on the upper side and the effective stiffness on the lower side. Shaded areas in blue and red indicate the bandgaps associated with the negativity of the effective mass and effective stiffness, respectively (For interpretation of the references to colour in this figure legend, readers are referred to the web version of this article).

Fig. 8. Complex frequency band structure of the dispersion curves of the spring-mass model to show the theoretical bandgap regions of metaconcrete including the real part on the upper side and the imaginary part on the lower side. Shaded areas in grey indicate the bandgaps (For

interpretation of the references to colour in this figure legend, readers are referred to the web version of this article).

Fig. 9. Bandgaps obtained from experimental test, prediction considering both the effective mass and effective stiffness, and prediction considering only the effective mass. Shaded areas in blue and red indicate the bandgaps associated with the comprehensive analysis and conventional analysis, respectively while the bandgaps from the experiment are denoted by the grey-shaded area (For interpretation of the references to colour in this figure legend, readers are referred to the web version of this article).

Fig. 10. Schematic view of the meta-truss bar used for modal analysis consisting of 8 unit cells in which each unit cells comprises of the outer shell (Al), two soft coatings (PU) and the two resonators (Al).

Fig. 11. Effective parameters of the spring-mass model with shear stiffness to show the theoretical bandgap regions of metaconcrete including the effective mass on the upper side and the effective stiffness on the lower side. Shaded areas in blue and red indicate the bandgaps associated with the negativity of the effective mass and effective stiffness, respectively (For interpretation of the references to colour in this figure legend, readers are referred to the web version of this article).

Fig. 12. Complex frequency band structure of the dispersion curves of the spring-mass model with shear stiffness to show the theoretical bandgap regions of metaconcrete including the real part on the upper side and the imaginary part on the lower side. Shaded areas in grey indicate the bandgaps (For interpretation of the references to colour in this figure legend, readers are referred to the web version of this article).

Fig. 13. Transmission coefficient against frequency of excitation for validation between numerical and analytical results. Shaded areas in blue and grey indicate the bandgaps associated with the analytical analysis and numerical analysis, respectively (For interpretation of the references to colour in this figure legend, readers are referred to the web version of this article).

Fig. 14. FFT spectra of the input and output displacements at center points of two ends of the meta-truss bar. Input prescribed displacement is applied to one end of the meta-truss bar while the output displacement is captured at the other end. The displacements of the input and output respectively denoted by the blue solid line and red dotted line are illustrated in (a) time histories and (b) FFT spectra. (For interpretation of the references to colour in this figure legend, readers are referred to the web version of this article).

Fig. 15. Flowchart of the meta-structure design consists 7 steps starting with the parameter initialization and ending with the meta-panel fabrication.

Fig. 16. Typical bandgap determination based on the dispersion curves is divided into three regions including [0-f_{11}] for the 1st bandgap, [f_{21}-f_{22}] for the 2nd bandgap, and [>f_{31}] for the 3rd bandgap. (For interpretation of the references to colour in this figure legend, readers are referred to the web version of this article).

Fig. 17. Peak impact force time history of the simulated impact loading generated by the impactor with the mass of 1kg and the velocity of 30 m/s.

Fig. 18. FFT spectrum of the impact force time history of the simulated impact loading F(t) generated by the impactor with the mass of 1kg and the velocity of 30 m/s.

Fig. 19. Estimated bandgap widths of the designed meta-truss bar including [0 – 4.8] kHz for the 1st bandgap, [7.5 – 8.5] kHz for the 2nd bandgap, and [>8.5] kHz for the 3rd bandgap. (For interpretation of the references to colour in this figure legend, readers are referred to the web version of this article).

Fig. 20. Dispersion curve of the designed meta-truss bar. Shaded areas in grey indicate the bandgaps (For interpretation of the references to colour in this figure legend, readers are referred to the web version of this article).

Fig. 21. Design of meta-panel including the schematic view of the meta-panel, meta-unit cell includes the outer tube, the coatings and the resonators, and meta-truss bar is made of 8 unit cells.

Fig. 22. Comparison of reaction force of the three panels under impact loading. Comparison of reaction force-time history of the back facesheet between the three considered meta-panels including meta-panel, the hollow-truss panel, and the solid-truss panel. (For interpretation of the references to colour in this figure legend, readers are referred to the web version of this article).

Fig. 23. Outline model utilized for the calculation of (a) k_2 and k_4, and (b) k_1 and k_3.

List of Tables